The Pennsylvania State University

The Graduate School

A COARSE-GRAINED MOLECULAR DYNAMICS MODEL OF THE MAMMALIAN NUCLEAR ENVELOPE

A Thesis in

Engineering Science and Mechanics

by

Pranjal Singh

Submitted in Partial Fulfillment
of the Requirements
for the Degree of

Master of Science

August 2021

The thesis of Pranjal Singh was reviewed and approved by the following:

Sulin Zhang
Professor of Engineering Science and Mechanics
Thesis Advisor

Francesco Costanzo
Professor of Engineering Science and Mechanics

Christian Peco
Assistant Professor of Engineering Science and Mechanics

Judith Todd
Professor of Engineering Science and Mechanics
Department Head of Engineering Science and Mechanics

Albert Segall
Professor of Engineering Science and Mechanics
Graduate Programs Officer of Engineering Science and Mechanics

ABSTRACT

The cell nucleus houses most of the genetic material in eukaryotic cells and is the site of many fundamental genome regulatory processes including cell division, gene expression, differentiation, and aging. The regulation of architecture of the nuclear envelope (NE) is essential for smooth operation of these processes. There is currently no physics-based model, theoretical or computational, which accounts for all significant interactions of subnuclear components in a common framework, leaving much of NE mechanics unexplored and poorly understood. We present a coarse-grained molecular dynamics model of the mammalian NE of unprecedented detail. A three-step protocol is shown to generate a coarse-grained nuclear envelope (CGNE) with experimentally consistent structure. The CGNE features a monolayer model of the nuclear membranes and a dynamically-linked meshwork model of the underlying nuclear lamina. Peripheral chromatin, which supports the meshwork from underneath and also interlaces with it, is modeled as a chain of mesoscale domains. The methodologies for *in silico* mechanical testing of the CGNE and extraction of metrics of NE viscoelasticity from the simulation data are described. Parameters are being tuned towards achieving experimental consistency of these viscoelastic properties. A revised CGNE model is planned to be published elsewhere in the near future.

TABLE OF CONTENTS

List of Tables

List of Figures

List of Abbreviations

2DV	Two-dimensional viscoelasticity (theoretical model)
CG	Coarse-grained
CGMD	Coarse-grained molecular dynamics
CGNE	Coarse-grained nuclear envelope
CL	Cross-link
CMF	Composite membrane fluctuations (theoretical model)
COM	Center of mass
FWHM	Full width at half maximum
LBP	Lamin-binding proteins
TL	Transverse-link
MW	Molecular weight
NE	Nuclear envelope
NL	Nuclear lamina
NL-A	A-type nuclear lamin meshwork
NL-B	B-type nuclear lamin meshwork
NM	Nuclear membrane
NP	Nuclear pore
NPC	Nuclear pore complex
PNS	Perinuclear space
SER	Stokes-Einstein Relation (theoretical model)
VCM	Viscoelastic contact mechanics (theoretical model)

Acknowledgements

I have been very fortunate to have the opportunity to work on an important problem in the field of nuclear mechanics. In 2018 when I started working on developing a model for the cell nucleus, I was inspired by lack of detailed models. During the 3 years, several papers emerged with unprecedented details of structural organization and mechanical properties resulting in a rich collection of experimental insights for modelling. I am therefore indebted to the scientific community at large which brought me the details which helped me in developing the model.

I am extremely grateful to my adviser, Dr. Sulin Zhang, who supported me in the project during several ups and downs. In 2019, the direction of the project became unclear. I had spread my simulations over a large amount of experimental data instead of completing one part of the problem at a time. In 2020, after substantial preliminary work in modelling of entire nucleus (which is not covered in this thesis), I finally brought my full focus on modeling of only the nuclear envelope (hence this thesis).

None of this would have been possible without the support of family and friends who continuously encouraged me to take care of myself amidst sleepless nights of exhaustion with failed simulations, and excitement with successful simulations.

I am deeply indebted to the head of ESM department, Prof. Judith Todd, for her valuable advice and supporting me through several teaching assistantships, and also to other ESM faculty and staff for assistance with degree process.

Chapter 1 Introduction

Background

Nuclear mechanobiology is an emerging field with interests in understanding the relationship of nuclear architecture i.e., structural organization of nuclear components, with the physical response of the nucleus to mechanical stimuli (Isermann and Lammerding 2013; Ungricht and Kutay 2017). The global deformation of the cell nucleus and local deformations in chromatin have been the topic of detailed investigation for many decades and have led to several insights in nuclear mechanics and mechanobiology. However, role of the nuclear envelope, which is present between the chromatin and nuclear periphery, had remained elusive until recent years. The regulation of architecture of the nuclear envelope (NE) occurs in many fundamental cellular processes including cell division, gene expression, differentiation, and aging (Ungricht and Kutay 2017). The nuclear lamina (NL), which is part of NE, has been suggested to contribute significantly to the mechanical stability and morphology of the NE (Webster, Witkin, and Cohen-Fix 2009). Diseases associated with NE are termed nuclear envelopathies and can result in abnormal function even in the absence of extreme external mechanical stimuli (Rowat et al. 2008). A major sub-category in this class of diseases is called laminopathies which involves abnormal expression and/or assembly of lamin isoforms e.g. in HGPS (Moller et al. 2009). On the other hand, extreme mechanical deformations of the nucleus may lead to abnormal NE mechanics e.g. detachment of the NL from the NM (Dahl et al. 2004) or formation of holes

in the NL (Deviri et al. 2019). Forces of physiological magnitude passing through the nuclear envelope can affect gene (Tajik et al. 2016).

Figure 1-1 illustrates the composition and structure of the mammalian nucleus and nuclear envelope. Structurally, the nuclear envelope is a multi-layered shell that encapsulates the genetic material of eukaryotic cells resulting in a membrane bound organelle known as the cell nucleus. Cryo-ET reconstruction of intact nuclear envelope has revealed a multilayered structure with unprecedented resolution (Mahamid et al. 2016; Turgay et al. 2017). The NE is composed of two layers: an outer layer called nuclear membrane (NM), and an inner layer called nuclear lamina (NL).

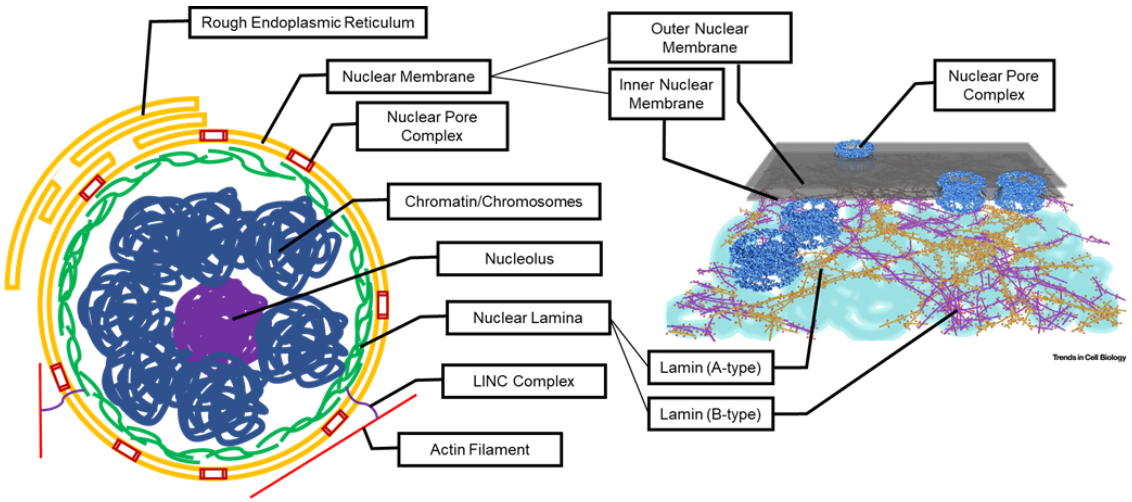

Figure 1-1. Illustrations of composition and structure of the mammalian nucleus (left) and nuclear envelope (right). The image on right was taken from (de Leeuw, Gruenbaum, and Medalia 2018) and used here only for illustrative purpose.

The NM comprises of two lipid bilayers bridged by molecular and topological entities. The inner (INM) and outer (ONM) nuclear membranes are lipid bilayers that are topologically fused sporadically forming nuclear pores (NP). Several proteins assemble in these pores forming the nuclear pore complex (NPC) and regulate nuclear transport. In addition, several transmembrane proteins integrated in the two bilayers participate in forming molecular bridges that have been implicated in maintaining an almost constant perinuclear space width (Cain et al. 2014; Cain and Starr 2015). Some transmembrane proteins bind the cytoskeletal structures to the NM, such as the nuclear envelope spectrin repeat proteins (Nesprins), some link nuclear lamina to the NM, such as the lamin B receptor (LBR) and Emerin, and some are involved in doing both, such as the SUN and KASH proteins combining into a linker of nucleoskeleton and cytoskeleton (LINC) complex. The ONM is also fused with lamellar structures known as the rough endoplasmic reticulum (RER). The RER is therefore extended regions of the ONM that act as lipid reservoirs.

The NL is a meshwork of type-V intermediate filament proteins underlying the NM. In mammalian nucleus, there are three lamin genes (LMNA, LMNB1 and LMNB2) that collectively express at least seven different protein isoforms which make most of the NL (Dechat et al. 2010). Based on their structural features, sequence homologies, expression patterns, and biochemical properties, lamin proteins are classified into A- and B-types. It is important to distinguish between the two types of lamins (A-type and B-type) due to the well documented distinction in their molecular structure (Dittmer and Misteli 2011), meshwork organization (Nmezi et al. 2019; Shimi et al. 2015) and mechanical

characteristics (Panorchan et al. 2004; Sengupta et al. 2013; Joe Swift et al. 2013). In vertebrates, lamin A and lamin C are two major isoforms of A-type lamins, and lamin B1 and lamin B2 are the major B-type lamin. As noted earlier, several proteins link the NL to the NM. In literature, they are collectively referred as lamin binding proteins (Wilson and Foisner 2010). Some of these proteins play a major role in force exchange between the cytoskeleton (CSK) and the NL and between the peripheral chromatin (PC) and the NL.

The nuclear interior comprises of chromatin-filled nucleoplasm. The interphase chromatin comprises of chromosomes occupying distinct territories in the nuclear interior. The nucleoplasm comprises of small biochemical species such as free/mobile proteins, ions and water.

Significance

In this section, literature is cited whereby biophysical characteristics of the nuclear envelope have been implicated in cellular functioning. These findings signify the importance of physical modelling of the NE.

Composition: Nuclear envelopathies such as Hutchinson-Gilford progeria syndrome (HGPS), Emery-Dreifuss muscular dystrophy (EDMD), dilated cardiomyopathy, Pelger Huetanomaly and familial partial lipodystrophy (FPLD) have been found to result from mutated and structurally aberrant NE proteins (Schreiber and Kennedy 2013). In addition to the biochemical signaling mechanisms, the pathological

mechanisms of envelopathies may involve biophysical mechanisms such as imbalance of the mechanical signaling due to abnormal changes in nuclear envelope structure (Osmanagic-Myers, Dechat, and Foisner 2015).

Viscoelasticity: Experimental characterization in nuclear mechanics has come a long way in the recent years with viscoelastic characterization of the nucleus (Guilak, Tedrow, and Burgkart 2000; Wintner et al. 2020) and its components (Panorchan et al. 2004; Sengupta et al. 2013). The comprehensive experimental data available now can be used for physical modelling of the NE viscoelasticity. Simulations performed with a model that is well-informed with literature can allow unprecedented accuracy in predicting dynamical events involved in NE mechanics.

Fracture: Tomographic slices of nuclear periphery show slender rod-like structures such as microtubules and F-actin poking the NE (Mahamid et al. 2016). It is surprising how the NE could protect the genetic material from external mechanical forces; given that it a perforated membrane, recall nuclear pores, atop a layer of randomly dispersed filamentous proteins. The microtubules, which are very sharp and stiff with $\sim 24\ nm$ diameter and $\sim 1400\ \mu m$ persistence length (van Mameren et al. 2009), have the potential to break the NE. They are indeed involved in breaking it during the nuclear envelope breakdown for cell division (Beaudouin et al. 2002). Physical modeling of the NE is a preliminary step for investigation of such processes.

Mechanobiology: While the interphase nucleus *somehow* protects itself against rupture, some forces acting on it may not be harmful and instead are *somehow* sensed by nucleus for gene regulation. A good amount of evidence has come up in the recent years that forces of physiological magnitudes can affect gene expression. When oscillatory surface shear force was applied to cells, a reversible stretching of chromatin and transcriptional upregulation of DHFR gene was observed (Tajik et al. 2016). A similar observation was made whereby reversible compaction of chromatin, when cells were compressed under coverslip, had implications on the accessibility of transcriptionally active genes (Damodaran et al. 2018).

Specific aims

The work presented in this thesis began with efforts to develop a model of the entire cell nucleus that will have enough details, e.g., separate nuclear membrane, nuclear lamina and chromatin, to study important diseases, such as cancer and HGPS, that are related to the nuclear mechanics. However, it became clear that the lack of a comprehensive model on the NE hinders such attempts. As such, this thesis aims to present a coarse-grained nuclear envelope (CGNE) model as a first step to facilitate modeling of NE in computational studies of nuclear mechanics in health and diseases. The development of the CGNE was broken down into a common 4-stage process in computational material science: conceptual modeling of the material based on experimental insights, computational structure generation, computational material characterization, and computational simulations. We describe below the aims/goals set for the first 3 stages, which is how far

we have reached in the process. In each stage, literature was thoroughly surveyed to collect experimental data for guidance and validation.

The first stage is developing a conceptual model. Hence, **Aim 1** was the conceptual formulation of the CGNE.

The second stage is generating a structure of CGNE. Hence, **Aim 2** was the development of a three-step protocol for (a) generating CGNE components, (b) assembling them into a CGNE structure with an *ad hoc* CGMD simulation, and (c) validating the CGNE structure with experimental data on the structural features of the mammalian NE in interphase cells.

The third stage is material characterization. This can be done by *in silico* mechanical testing of the 'CGNE structure' obtained in ***Aim 2***. However, before we set the aim for the third stage, consider first the following issue of *tunable parameters* in our model. The experimental consistency of the structural features of the CGNE structure cannot sufficiently guarantee validity of chosen values of the model parameters used to achieve the structure. Fortunately, with the continual innovations of experimental techniques and significant interest in nuclear mechanics, several articles could be found with experimental characterization of molecular interactions and we used these insights while choosing several parameters. Nevertheless, several types of interactions that our model includes are yet to be characterized experimentally. We refer the parameters of such interaction models as *tunable parameters* of our model. We will identify and discuss the

tunable parameters later in the thesis. Returning to setting the aim for the third stage, **Aim 3** was obtaining (a) viscoelastic properties of the CGNE via *in silico* mechanical testing (b) better choices of the *tunable parameters* by seeking consistency of the values with experimental estimates.

Thesis organization

In this chapter, the work was introduced with background, significance, and specific aims. In this last section we describe the organization of thesis.

In Chapter 2, ***Aim 1*** is addressed and conceptual framework for ***Aim 2 and Aim 3*** is described. There, we cover the CG modeling of the NE, conceptual framework for assembling and validating CGNE structure, and conceptual framework for characterizing and validating viscoelasticity of the CGNE. The organization of the simulation package is also outlined.

In Chapter 3, ***Aim 2*** is addressed. There, we present a protocol that results in a CGNE structure that is representative of the mammalian NE in interphase cells.

In Chapter 4 and Chapter 5, progress on ***Aim 3*** is presented. Due to (a) dozens of parameters currently being tuned and (b) simulation time for testing a revised parameter set ranging from 5 to 10 hours, it has become clear that the time is insufficient to complete the iterative process of parameter tuning. Hence, we have decided to present the

methodology but exclude the results – as they are not publication ready. In Chapter 4, we present methodologies for *in silico* mechanical testing of the CGNE and extraction of metrics of NE viscoelasticity from the simulation data. In Chapter 5, we present our progress on choices of the parameters.

In Chapter 6, we discuss the contributions of other works to our model, and the limitations of those works that our model overcomes *by design*.

In Chapter 7, the thesis is concluded with comments on future work, notably the ongoing parameter tuning.

This concludes the thesis organization. The reader may refer to the first paragraph of each chapter for organization of the content in each chapter.

Chapter 2 Conceptual framework

This chapter has six sections covering in total the CG modeling of the of the NE, and conceptual frameworks of structure generation and viscoelastic characterization of the CGNE. The first three sections are on CG modeling of the NE. In the first section, *Modeling from experimental insights* is discussed whereby a CG model of the NE is conceptualized from experimental knowledge. In the second section, the simulation method of *Coarse-grained molecular dynamics* is described. In the third section, the *Interaction models* are described which will serve as models of physical interactions of various components of the CGNE during the simulations. The fourth section describes the approaches for *Structural assembly and validation* of the CGNE structure. The resulting 'CGNE structure' represents the equilibrium NE structure to be used as initial configuration in the CGMD simulations. The fifth section describes the approaches for *Viscoelastic characterization* of the CGNE. Finally, the sixth section outlines the organization of the simulation package.

Modeling from experimental insights

In this section, we present a CG model of the NE of unprecedented detail. Through this section, we hope to convey both the features and limitations of our model at a conceptual level. In particular, we highlight the decisions made to preserve or simplify experimental details on composition, interaction, molecular structure, and supramolecular organization of NE components which resulted in the CGNE.

Simplification of NE composition: We will consider the NE comprising of four components: NM, NPC, NL-A and NL-B as introduced in Chapter 1. The first two components will be described with a monolayer of particles, while the last two will be described together as a meshwork of filaments. Peripheral chromatin (PC), which supports the meshwork from underneath and also interlaces with it, will be modeled as a chain of mesoscale domains (Miron et al. 2020). Each of the monolayer, meshwork and chain will be two-component. The model will therefore comprise in total of the following 6 particle types (Figure 2-1):

1. Monolayer with
    a. Type 1 (NM) particles, each covering approximately $355\ nm^2$ region of the nuclear membrane, and
    b. Type 2 (NPC) particles, each representing a single nuclear pore complex,
2. Meshwork with
    a. Type 3 (NL-A) particles representing globular domains on A-type nuclear lamin filaments, and
    b. Type 4 (NL-B) particles representing globular domains on B-type nuclear lamin filaments, and
3. Chain with
    a. Type 5 (EC) particles representing Euchromatin regions of peripheral chromatin, and
    b. Type 6 (HC) particles representing Heterochromatin regions of peripheral chromatin.

Note that in traditional nomenclature, PC does not constitute the NE. However, due to experimental evidence of its physical associativity and interlacing with NE components, we incorporate PC in our model for simulating NE mechanics.

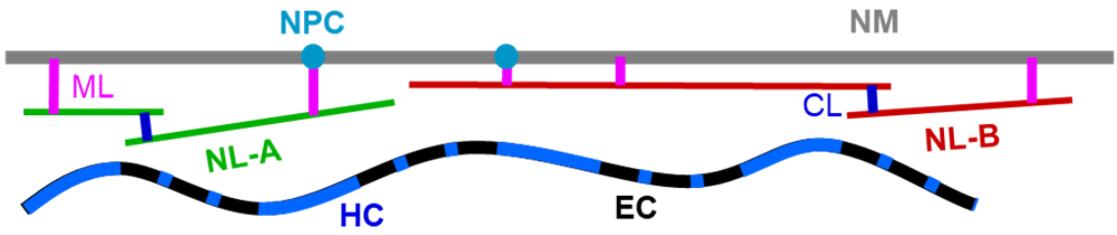

Figure 2-1 Illustration of the NE with a simplified composition of 6 components: NM, NPC, NL-A, NL-B, EC, and HC. The CL and TL are transient structures that represent cross-linking within NL and transverse-linking of NL to NM and NPC.

Simplification of interactions of NE components: The mathematical form of the interactions will be described in the next two sections. Here we outline the simplifications in choosing potentials for modeling interactions across the monolayer, meshwork and chain (Table 2-1).

We consider first the non-bonded interactions. Since the monolayer shall represent a fluid membrane, interaction of particles will be purely non-bonded and will be achieved with the *Membrane potential*. A few particles in the monolayer will be identified as NPC and the rest as NM. This naturally recapitulates the experimental observation that the NM is embedded with NPCs. Being two-component, the monolayer requires 3 interactions to be defined: NM-NM, NM-NPC, and NPC-NPC. For the first and second, the *Membrane*

potential is used. The first usage will keep the NM particles assembled as a monolayer. The second usage will keep NPC assembled in the monolayer. For the third, the *Mie potential* will be used for steric repulsion of NPC particles, preventing them from forming patches of fused NPCs not common in healthy nuclei. In fact, the *Mie potential* will be used for all remaining non-bonded interactions due to its versatility; discussed later in third section. Hence, the *Mie potential* will model NM-NL and NL-NL attraction (which occurs when CLs or TLs begin to form) and repulsion (which occurs when particles come too close but couldn't bond). The *Mie potential* will also model NM-PC and NL-PC attraction (which represents binding of DNA to INM and lamins) and repulsion (which occurs when NM and NL particles come too close causing steric repulsion). Finally, the *Mie potential* will also model associativity and steric repulsion within the PC.

Five types of bonded interactions are included, with reversible bonding in two types of interactions. Experimentally, the force-extension behavior of single lamin dimer is saw-tooth like due to several molecular events such as protein unfolding and conformational change (Bera et al. 2014). However, assembled lamin oligomers have several intramolecular associations that may result in a smooth, although non-linear, force extension behavior (Makarov et al. 2019). A multi-polynomial (non-linear) potential has been developed that produced consistent results in simulations and AFM experiments on stretching of lamins under 3-point bending (Sapra et al. 2020). It can be noted in that article that nonlinearity can be ignored up to 50% strain. While the highly localized loading of NL filaments *in vitro* revealed behavior beyond 50% strain, we do not expect such large strains localized on individual lamin filaments *in vivo*. Hence, we consider only the first branch

relevant in our model. This simplification will, of course, need verification that the maximum strain is indeed within the first branch. If not, further branches of the potential will need to be used. Therefore, the NL filaments will have type A bonds maintaining *stiff* connectivity of particles, and type A angular bonds to provide *semiflexibility* i.e., bending resistance. The *Harmonic potential* will be used for type A bonds and the *Cosine potential* will be used for type A angular bonds. Experimentally, the PC chain is *finite-extensible* and *freely-joint*. Therefore, the PC chain will have a type D bond with *finite-extensibility*, but will not have angular bonds. The *Kremer-Grest potential* will be used for type D bonds. The physical linking of the NL filaments with each other is *weak* and *reversible*. Therefore, the meshwork will have cross-links (CLs), also referred as type B bonds. The *Morse potential* will be used for the *weak* connectivity of the type B bonds, and *reversibility* will be achieved via the *Break* and *Create* procedure. A class of proteins referred as lamin-binding proteins (LBPs) are involved in linking of lamins with INM. Some of these binding interactions are transient, while some are stable (Wilson and Foisner 2010). Due to the current lack of detailed experimental data on binding strength and reversibility of various LBPs, we will take a conservative approach in modeling the role of LBPs by including *weak* and *reversible* transverse-links (TLs), also referred as type C bonds. Similar to type B bonds, the *Morse potential* will be used for the *weak* connectivity, and *reversibility* will be achieved via the *Break* and *Create* procedure. Experimentally, DNA has also been observed to bind with lamins and INM through several binding proteins. In fact, nuclear envelope transmembrane proteins (NETs) is a class of proteins involved in binding of lamins, DNA and INM; LBPs is a sub-class of this broader class of proteins. Yet, we do not include transverse-linking or cross-linking of the PC particles with NM and NL

particles in our model. This is because each PC particle is a coarse-grained region with several sites for DNA binding. As such, the location of bound DNA would be poorly resolved (within a 70 nm wide spherical region) by the PC particle in the chain. Instead, we consider that the weak associativity of the PC particles with neighboring NM and NL particles through non-bonded interactions (*Mie potential*) may serve as simplified models of the binding of DNA with lamins and INM. Nevertheless, there is currently a lack of detailed experimental data on binding strength and reversibility of various NETs to guide explicit modeling of binding of DNA, lamins and INM.

Table 2-1 Models of various types of interactions of the NE components.

Interaction	**Model**
Non-bonded interactions	
NM – NM	Membrane
NM – NPC	Membrane
NPC – NPC	Mie
NL – NL	Mie
PC – PC	Mie
(NM, NPC) – NL	Mie
(NM, NPC) – PC	Mie
NL – PC	Mie
Bonded interactions	
NL filament connectivity	Harmonic
Cross-link (CL)	Morse
Transverse-link (TL)	Morse
PC chain connectivity	KG
NL filament bending	Cosine
Reversible bonding	
CL	Create procedure
TL	Create procedure
CL	Break procedure
TL	Break procedure

Simplifications in representing NPC-embedded NM: Strictly speaking, the NM is not a particle monolayer and the approach taken here may seem an extreme simplification of the structure. Indeed, the actual 'nuclear membrane' is two lipid bilayers connected sporadically via topological fusion (nuclear pores (NPs)) and molecular bridges (protein complexes spanning the perinuclear space (PNS)). However, consider these statements:

a) The NPs are stuffed with NPCs that span the two membranes and locally constrain the PNS width (Beck et al. 2007; Jahed et al. 2016).

b) The molecular bridges also span the two membranes and locally constrain the PNS width (Cain et al. 2014; Cain and Starr 2015).

If tracking the motion of lipids on individual bilayers is not of interest, the above suggests that explicit modeling with individual membranes may not be necessary. We hypothesize that despite being a CG representation of the NM, the particle monolayer model can capture its roles as (a) an elastically deformable barrier to mixing of nucleoplasm and cytoplasm, (b) a viscous layer in which giant protein assemblies (such as NPC) float, and (c) a surface on which lamins form a meshwork called NL (with some interlacing PC). In direct comparison, we consider that the particle monolayer is a discrete representation of the imaginary mid-surface of the actual NM between the two leaflets (INM and ONM) (Figure 2-2a). Drawing the Connolly surface of NPC-excluded NM monolayer makes this obvious. The Connolly surface visualizes the leaflets along with NPCs residing in the nuclear pores.

Simplifications in representing NL: A lamin dimer consists of two globular domains (red) and rod domain (grey) and the actual 'NL filament' comprises of

longitudinally and laterally assembled lamin dimers (Figure 2-2b), (Turgay et al. 2017). In direct comparison, a NL particle represents two globular domains and a NL filament bond represents the half-staggered rod domain in between (Figure 2-2b). The NL is then a meshwork resulting from supramolecular organization of these filaments. Note that we actually consider two meshworks forming the NL. Indeed, NL-A constitutes A-type NL filaments and NL-B constitutes B-type lamin filaments. Interestingly, NL-A and NL-B filaments are found to form separate microdomains (Shimi et al. 2008) suggesting apparent immiscibility in the context of polymer blending. Knockdown of lamin B1, a B-type lamin, has also been observed to result in aberrant mesh size of NL-A (Shimi et al. 2008, 2015). A disappearance of NL-B, and not NL-A, from highly curved regions of NE has also been observed (Nmezi et al. 2019). Furthermore, NL-B is found to be closer to the NM than NL-A (Nmezi et al. 2019). The molecular structure of A- and B-type lamins has a notable distinction that B-type lamins have a farnesyl group, which is known to impart high membrane binding affinity to proteins (Dittmer and Misteli 2011). These experimental observations on distinctions in the molecular structure and supramolecular organization underscore potentially distinct contributions of the NL-A and NL-B in the NE. Hence, we consider the two meshworks distinctly so that their distinct, similar, and synergistic interactions can be appropriately represented.

Simplifications in representing associations of NM and NL: Transient associations form in the NL and NM due to physical associativity of globular domains on lamins (CLs), and binding of lamins to NM (TLs).

Mature lamins (except lamin C, an A-type lamin) form through post-translational modifications of the -CAAX box in 'pre-lamins', which contains a farnesyl group. The farnesyl group is removed in A-type and preserved in B-type. Lamin C, which is 74 residues shorter than mature lamin A, does not possess a –CAAX box to begin with and is therefore not farnesylated or modified. The closeness of the B-type lamins to the NM than the A-type lamins is a potential consequence of this distinction since farnesyl group shows strong membrane-binding affinity (Nmezi et al. 2019). Since the *self-linking* interaction of NL-B is non-specific (a B-type lamin 'bound' to NM this was can remain bound during long-range sliding), this mechanism will be incorporated by using a stronger non-bonded interaction of NL-B with NM, than that of NL-A with NM. Returning to NL-A, note that permanent retention of farnesyl group or no farnesylation at all in A-type lamins can induce pathological abnormalities in NE (Capell et al. 2005). Proteins in the NM (such as LBPs (Schmidt et al. 2013; Wilson and Foisner 2010)) or the NPC (such as Nucleoporins (Kittisopikul et al. 2021)) play a major role in binding the A-type lamins (and also B-type lamins). Since the linking via these proteins is site-specific (long-range sliding of the lamin bound this way will pull on a specific NM particle or NPC), this mechanism requires bonded interaction. Therefore, we included TL as model of lamins bound to NM via LBPs (Figure 2-2c).

Observations of thick lateral bundles of nuclear lamins *in vitro* and *ex vivo* had led to a hypothesis that the globular domains may participate in lateral interactions of filaments, otherwise known as cross-linking (Moir, Donaldson, and Stewart 1991). Since bundling is rare *in vivo*, it has been speculated that the cross-links are weak and reversible.

Recent experiments have provided evidence supporting this speculation: SILAC-CLMS (Makarov et al. 2019) and SEC-MALS (Ahn et al. 2019) experiments have shown the wrapping of electrostatic potential surfaces (EPS) as a physical cross-linking mechanisms of longitudinal and lateral assembly. In the SILAC-CLMS experiments, direct examination of the longitudinal lamin assembly stages with rotary metal shadowing EM revealed an increase in free lamin A dimers relative to the tetramers and oligomers in diseased nuclei relative to wild type. The electrostatically-driven head-to-tail assembly was explained to be blocked in diseased nuclei due to mutations. Finally, lateral interaction i.e., cross-linking of lamin filaments in rat liver NE *ex vivo* supported physical cross-linking via electrostatic interactions. These results suggest that cross-linking is not only important for the oligomeric assembly of dimers into filaments but continues (although as a weaker physical interaction) towards intermolecular assembly of filaments into the NL. Therefore, we include CL as model of physically associated globular domains on lamins (Figure 2-2d).

Simplifications in representing PC: As no model, theoretical or computational, exists with distinct NL and NM, we initially considered excluding PC from our model; just modeling NL and NM seemed a significantly involved problem. However, it is well known that the PC is long chains that intermingle with NL, forming lamina-associated domains (LADs) (Guelen et al. 2008; Kind et al. 2013; van Steensel and Belmont 2017; Ulianov et al. 2019). Until 2020, we incorporated a minimal role of chromatin in supporting the NL from beneath via a purely repulsive wall. However, this handicapped our model due to the absence of the PC interlacing the NL. For a model that attempts to do a comprehensive inclusion of all physical interactions relevant to NE mechanics, the evidence on reduced

nuclear viscoelasticity upon disruption of LADs (Discher et al. 2007; Schreiner et al. 2015; Ulianov et al. 2019) was too strong to continue ignoring explicit modeling of PC for modeling convenience.

As described in third section of Chapter 1, the work presented here excludes our broader work done towards modeling of the entire nucleus. During these early studies and preliminary simulations, we had come across the Kreme-Gerst (KG) potential (which is a combination of FENE bond for worm-like entropic elasticity, and WCA potential for steric repulsion) which when combined with identification of strongly associating heterochromatin (HC) regions and weakly associating euchromatin (EC) regions on the chromatin was a model sufficient for reproducing experimental chromatin folding and organization (Bianco et al. 2018; Lieberman-Aiden et al. 2009). However, in 2018, we left considerations of incorporation of this model as we couldn't find experimental clues on how PC interacts with NL. Fortunately, in 2020, we came across an article which showed how this model could be used to produced experimentally relevant LADs and TADs (Chiang et al. 2019). With the capabilities of this model well demonstrated in the article, we will use it to introduce PC as a chain of mesoscale domains with HC and EC regions (Figure 2-2e).

Note that our model of NE is a dynamic two-component monolayer with an underlying two-component meshwork, instead of a static single-component monolayer in that article. Due to this, we will have more detailed NE-EC and NE-HC interactions to be defined (NM-EC, NM-HC, NPC-EC, NPC-HC, 'NL-A'-EC, 'NL-A'-HC, 'NL-B'-EC, and

‘NL-B’-HC) beyond those presented in that article (only NE-EC and NE-HC; referred in the article as NL-EC and NL-HC interactions). We will simplify the process of defining the detailed interactions as follows: We will carry over the ratio of strength (i.e., ratio of depth of potential well) of NE-HC, HC-HC, HC-EC, EC-EC, and EC-NE interactions from the AC region (healthy phase space). To carry over the NE-EC and NE-HC interactions, we will use molecular dynamics combining rules, e.g., Lorentz-Berthelot rules, to guess the interaction strength ϵ of the detailed interactions NM-EC, NM-HC, NPC-EC, NPC-HC, ‘NL-A’-EC, ‘NL-A’-HC, ‘NL-B’-EC, and ‘NL-B’-HC from the coarse-grained interactions NE-EC and NE-HC. This process does not guarantee unique determination of the model parameters, and is indeed not mathematically rigorous. At the moment of preparing this thesis, the author has not come across experimental data for clues on relative strength of these interactions. Re-tuning of these parameters with experimental clues is a major area of improvement, but has to be left as future work. For the present work, we use the ad hoc parameter values, guessed via the process, as temporary guesses so as to simulate CGNE and compare its viscoelasticity with experimental data. Much of the work presented in this thesis is a work in progress with iterative improvement of the model based on search-and-use of experimental data. While we continue to look for literature data to improve our choices of model parameters, whether it will be found anytime soon remains an unknown.

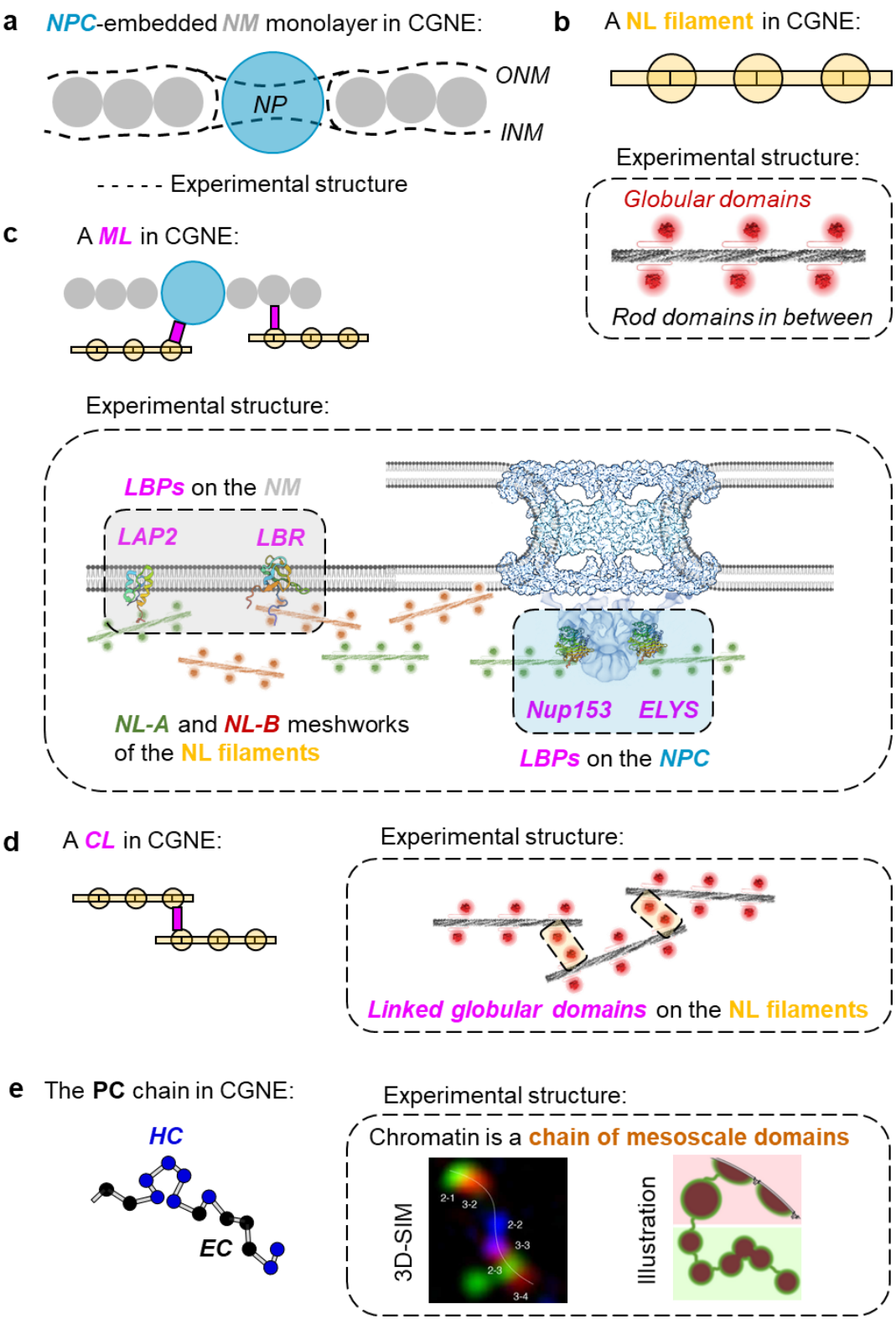
a
NPC-embedded NM monolayer in CGNE:
NP
ONM
INM
Experimental structure
b
A NL filament in CGNE:
Experimental structure:
Globular domains
Rod domains in between
c
A ML in CGNE:
Experimental structure:
LBPs on the NM
LAP2
LBR
NL-A and NL-B meshworks
of the NL filaments
Nup153
ELYS
LBPs on the NPC
d
A CL in CGNE:
Experimental structure:
Linked globular domains on the NL filaments
e
The PC chain in CGNE:
HC
EC
Experimental structure:
Chromatin is a chain of mesoscale domains
3D-SIM
2-1
3-2
2-2
3-3
2-3
3-4
Illustration

Figure 2-2 Coarse-grained structure of NE components. **a,** The NPC-embedded NM is modeled as a particle monolayer. The experimental structure of the NPC-embedded NM is illustrated in **c**; it can also be imagined as the Connolly surface that wraps the monolayer when NPC is excluded. **b**, The ball-and-stick model of a NL-A and NL-B filaments. The balls cover the globular domains and sticks cover the rod domains. The experimental structure was taken from (Turgay et al. 2017) and used here only for visual comparison. **c**, The TLs are simplified representations of the LBPs on the NM and NPC. The illustrations of proteins are from the Protein Data Bank (PDB) (Burley et al. 2021). **d**, The CLs are simplified representations of the physically linked globular domains on the NL filaments. **e**, The chain-of-bead model of EC and HC regions of PC. The 3D-SIM image and illustration were taken from (Miron et al. 2020) and used here only for visual comparison.

Coarse-grained molecular dynamics

In this section, we describe the method to be used for simulating dynamics of the CGNE.

Equations of motion: Lamins and chromatin are submerged in nucleoplasm, and the NM is partially submerged in both cytoplasm and nucleoplasm. The particles in the CGNE shall therefore be subject to random and frictional forces from a background solvent. Langevin dynamics is used to implicitly incorporate such fluctuation-dissipation effect of the solvent via a stochastic (randomly fluctuating) force and a frictional (dissipative) force on each particle (Allen and Tildesley 2017). The equation of motion for the time evolution of the position of each particle's center of mass, $\boldsymbol{r}_i$ is:

$$m_i \frac{d^2 \boldsymbol{r}_i}{dt^2} = -\boldsymbol{\nabla}_{\boldsymbol{r}_i} U_i - \gamma_{t_i} \frac{d\boldsymbol{r}_i}{dt} + \sigma_{t_i} \boldsymbol{\psi_t}(t)$$

where, m_i and U_i are the mass and total potential energy of the particle respectively. The translational friction coefficient, γ_{t_i} is defined as $\frac{m_i}{\tau_t}$ where τ_t is relaxation time for linear (translational) momentum i.e., time taken for the velocity of a particle to decay to $\frac{1}{e} \approx 0.368$ of original velocity under background friction. The coefficient σ_{t_i} governs the strength of the stochastic forces and is related to γ_i through the fluctuation-dissipation theorem as $\sigma_{t_i} = \sqrt{2\gamma_{t_i} k_B T}$, where, k_B is the Boltzmann's constant and T is the temperature of the solvent. $\boldsymbol{\psi_t}(t)$ is a randomly oriented unit vector for the stochastic forces. The monolayer particles additionally have their orientations, $\boldsymbol{n}_i$ as part of the generalized coordinates being tracked. The equation of motion for the time evolution of orientation of a body-fixed vector on these particles, $\boldsymbol{n}_i$ is:

$$I_i \frac{d^2 \boldsymbol{n}_i}{dt^2} = -\boldsymbol{\nabla}_{\boldsymbol{n}_i} U_i - \gamma_{r_i} \frac{d\boldsymbol{n}_i}{dt} + \sigma_{r_i} \boldsymbol{\psi_r}(t)$$

where, I_i is the moment of inertia, $\gamma_{r_i} = \frac{I_i}{\tau_r}$ is the rotational friction coefficient with τ_r as the relaxation time for angular (rotational) momentum, $\sigma_{r_i} = \sqrt{2\gamma_{r_i} k_B T}$ governs the strength of the stochastic torques, and $\boldsymbol{\psi_r}(t)$ is a randomly oriented unit vector for the stochastic torques. For simplicity, we consider the monolayer particles to be spherical. Therefore, $I_i = \frac{2}{5} m_i R_i^2$, where, R_i is the chosen particle radius. The choice of parameters in above equations (m_i, τ_t, τ_r R_i and T) will be discussed in Chapter 5, along with choice of parameters in the interaction potentials that contribute to U_i when summed over.

Simplification of interaction potentials: For a system of N particles interacting through non-bonded and bonded interactions in absence of gravity (which can be assumed for small systems), the total potential energy of the particle, U_i has the form $U_i = U_i^{non-bonded} + U_i^{bonded}$. The non-bonded term has the general form $U_i^{non-bonded} = \sum_{j\neq i} U_{ij} + \sum_{j\neq i}\sum_{k\neq j} U_{ijk} + \cdots$. The customary pairwise approximation $U_i^{non-bonded} \approx \sum_{j\neq i} U_{ij}^{eff}$ gives remarkably good description of liquid properties (Allen and Tildesley 2017). It is therefore utilized for monolayer particles. Meshwork filaments are loosely packed and therefore terms involving three-body or higher coordination are neglected. Hence, we use $U_{ij}^{Membrane}$ as U_{ij}^{eff} for the non-bonded interactions maintaining the monolayer (NM-NM and NM-NPC interaction), and U_{ij}^{Mie} as U_{ij}^{eff} for all the remaining non-bonded interactions. The bonded term for polymers usually has the general form $U_i^{bonded} = \sum_j U_{ij}^{stretching} + \sum_j \sum_k U_{ijk}^{bending} + \sum_j \sum_k \sum_l U_{ijkl}^{dihedral} + \sum_j \sum_k \sum_l U_{ijkl}^{improper}$. Since the NL filaments are linear and semiflexible, we ignore the dihedral and improper terms. We use $U_{ij}^{Harmonic}$ as $U_{ij}^{stretching}$ and U_{ijk}^{Cosine} as $U_{ijk}^{bending}$ for NL filament connectivity and bending. Since the PC chain is a freely-joint chain (FjC) of coarse-grained beads, the bending term is further neglected. We use U_{ij}^{KG} as $U_{ij}^{stretching}$ for the PC chain connectivity. The CL and TL are individual links between particles. Hence, we neglect the bending, dihedral and improper terms and use U_{ij}^{Morse} as $U_{ij}^{stretching}$.

Interaction models

In this section, the mathematical forms of the interaction potentials used for coarse-grained representation of the physical interactions of neighboring (non-bonded) and connected (bonded) particles are described.

Membrane potential: A one-particle-thick, solvent-free, coarse-grained model for biomembranes will be used which utilizes an anisotropic pairwise potential (Yuan et al. 2010). In this potential, the strength of interaction is weighed by the relative particle orientations allowing a simple approach to model bending rigidity in a monolayer, rendering it a one-particle-thick membrane model. The potential is described as follows:

$$U_{ij}^{Membrane} = \begin{cases} u_R(r) + \left[1 - \varphi\left(\hat{\boldsymbol{r}}_{ij}, \boldsymbol{n}_i, \boldsymbol{n}_j\right)\right]\varepsilon, & r < r_{min} \\ u_A(r)\varphi\left(\hat{\boldsymbol{r}}_{ij}, \boldsymbol{n}_i, \boldsymbol{n}_j\right), & r_{min} < r < r_c \end{cases}$$

where, $u_R(r) = \epsilon\left[\left(\frac{r_{min}}{r}\right)^4 - 2\left(\frac{r_{min}}{r}\right)^2\right]$ is the pairwise-distance-dependent repulsive interaction potential, $u_A(r) = -\epsilon\, cos^{2\zeta}\left[\frac{\pi}{2}\frac{r - r_{min}}{r_c - r_{min}}\right]$ is the pairwise-distance-dependent attractive interaction potential, and $\varphi\left(\hat{\boldsymbol{r}}_{ij}, \boldsymbol{n}_i, \boldsymbol{n}_j\right) = 1 + \mu[\left(\boldsymbol{n}_i \times \hat{\boldsymbol{r}}_{ij}\right) \cdot \left(\boldsymbol{n}_j \times \hat{\boldsymbol{r}}_{ij}\right) + \sin\theta_0\left(\boldsymbol{n}_j - \boldsymbol{n}_i\right) \cdot \hat{\boldsymbol{r}}_{ij} - \sin^2\theta_0 - 1]$ is the orientation-dependent interaction potential. Also, $r = \left\|\boldsymbol{r}_{ij}\right\|$ is the pairwise distance between particles i and j, r_{min} (set to $\sqrt[6]{2}\,\sigma$ without loss of generality) is the distance at the minimum of the potential, and r_c is the cut-off for the interaction. The parameters ϵ, σ, r_c, ζ, μ and θ_0 tune the dissociation energy, pairwise separation, secondary neighbor interaction, particle momentum

diffusivity, membrane bending resistance and spontaneous curvature of the membrane, respectively.

Mie potential: The Mie potential will be used to model the repulsive and attractive interactions between two particles (Israelachvili 2011). The potential is described as follows:

$$U_{ij}^{Mie} = \begin{cases} -\frac{A}{r^n} + \frac{B}{r^m} & r < r_c \\ 0 & r \geq r_c \end{cases}$$

where, $A = C\epsilon\sigma^n$ and $B = C\epsilon\sigma^m$ are chosen with $C = \left(\frac{m}{m-n}\right)\left(\frac{m}{n}\right)^{\frac{n}{m-n}}$ so that $\{m,n\} = \{12,6\}$ corresponds to standard Lennard-Jones potential and $\{m,n\} = \{4,2\}$ corresponds to the soft-core Lennard-Jones potential, $u_R(r)$ used in the Membrane potential, $U_{ij}^{Membrane}$. Again, $r = \|\boldsymbol{r}_{ij}\|$ is the pairwise distance between particles i and j. Note that the equilibrium separation is given by $r_{min} = \left(\frac{m}{n}\right)^{\frac{1}{m-n}}\sigma$ and the stiffness of the potential close to r_{min} is given by $K = \frac{m\,n\,\epsilon}{r_{min}^2}$. The parameters ϵ, σ, r_c, m and n tune the dissociation energy, pairwise separation, secondary neighbor interaction, strength of repulsion, and strength of attraction, respectively.

Harmonic potential: A linear spring will be used to model elastic connectivity of two bonded particles:

$$U_{ij}^{Harmonic} = \frac{1}{2}K(r - r_0)^2$$

where, $r = \|\boldsymbol{r}_{ij}\|$ is the pairwise distance between particles i and j. The parameters K and r_0 are material parameters that correspond to the extensional stiffness of spring and the equilibrium separation, respectively.

Morse potential: A nonlinear spring will be used to model non-linear elastic connectivity of two bonded particles:

$$U_{ij}^{Morse} = \begin{cases} D_0\left(1 - e^{-\alpha(r-r_0)}\right)^2 & r < r_{brk} \\ 0 & r \geq r_{brk} \end{cases}$$

where, $\alpha = \sqrt{\frac{K}{2D_0}}$ is chosen so that $\lim_{r \to r_0}\left(U_{ij}^{Morse}\right) = U_{ij}^{Harmonic}$. Again, $r = \|\boldsymbol{r}_{ij}\|$ is the pairwise distance between particles i and j. The parameters D_0, K and r_0 are material parameters that correspond to the bond dissociation energy, the stiffness of spring close to equilibrium separation, and the equilibrium separation, respectively. Making the bond at r_{mk} and breaking it at r_{brk} will be enforced by the *Create* and *Break* procedures discussed later.

Cosine potential: A three-body Kratky-Porod potential models the local bending stiffness of a filament at particle i between particles j and k:

$$U_{ijk}^{Cosine} = \frac{L_p\, k_B T}{r_0}\left(1 - \cos(\theta_i - \theta_0)\right)$$

where, $\theta_i = \frac{\boldsymbol{r}_{ij} \cdot \boldsymbol{r}_{ik}}{\|\boldsymbol{r}_{ij}\|\|\boldsymbol{r}_{ik}\|}$. The parameters L_p and θ_0 are material parameters that correspond to the persistence length of the filament and equilibrium angle at particle i,

respectively. Note that the particle i is the middle particle in the angle formed by the three particles.

Kremer-Grest potential: A finite-extensible nonlinear-elastic (FENE) spring will be used to model the entropic elasticity of the folded chromatin between the bonded PC particles during extension, and a purely repulsive Weeks-Chandler-Anderson (WCA) will be used to model the steric repulsion during compression:

$$U_{ij}^{KG} = \begin{cases} -\frac{kR^2}{2} ln\left[1 - \left(\frac{r}{R}\right)^2\right] + 4\epsilon\left[\left(\frac{\sigma}{r}\right)^{12} - \left(\frac{\sigma}{r}\right)^{6} + \frac{1}{4}\right] & r < 2^{1/6}\sigma \\ -\frac{kR^2}{2} ln\left[1 - \left(\frac{r}{R}\right)^2\right] & r \geq 2^{1/6}\sigma \end{cases}$$

where, $r = \|\boldsymbol{r}_{ij}\|$ is the pairwise distance between particles i and j. The parameters K, R, ϵ and σ tune extensional stiffness, maximum extension, strength of repulsion and equilibrium distance of the bond.

Reversible bonding: A reversible bonding algorithm will be used for the weak bonds (modeled with *Morse potential*) to model their breaking when the bond yields (*Break* procedure), and their formation when eligible particles are close enough (*Create* procedure).

The Break procedure can be described as following: Break bonds of selected bond type between pairs of particles of the selected type with a probability p and at a frequency f_{brk} if the bond is stretched beyond r_{brk}.

The Create procedure can be described as following: Create bonds of selected bond type between pairs of particles of the selected type with a probability p and at a frequency

f_{mk} if the pair separation, r_{ij} is within r_{mk}, allowing a maximum of i_{max} bonds of the selected bond type on ith particle and a maximum of j_{max} bonds of the selected bond type on jth particle.

The parameter set for Break procedure is $\{f_{brk}, r_{brk}, p\}$ and that for Create procedure is $\{f_{mk}, r_{mk}, i_{max}, j_{max}, p\}$.

Structural assembly and validation

In this section, we conceptualize a three-step protocol for (a) generating positions and orientations of CGNE components, (b) assembling them into a CGNE structure with an *ad hoc* CGMD simulation, and (c) validating the CGNE structure with experimental data on the architecture and morphology of the mammalian NE in interphase cells. It is important to remark here that while the second step in the protocol described here involves a simulation of NE assembly, it is only an *ad hoc* simulation developed for conveniently obtaining an assembled NE structure from the initially generated configurations of the CGNE components. The actual NE assembly, which is a very sophisticated and poorly understood process (Ungricht and Kutay 2017), may be different than the *ad hoc* simulation.

Step 1: The monolayer will be generated as a 2D triangular lattice in the xy-plane with a fraction of lattice sites randomly allocated with NPC and rest with NM. All the monolayer particles will be oriented in positive z-direction. The meshwork will be generated as a collection of NL-A and NL-B filaments grown below the monolayer in the

negative z-direction at random but equally spaced locations. The chain will be generated as a random walk with a few nodes allocated with HC and the rest with EC. Pseudo-random number generators (PRNGs) will be used for ensuring each configuration is random, but reproducible.

Step 2: The three configurations will be combined into a common simulation box and an assembled NE structure will be obtained through an *ad hoc* CGMD simulation in 5 stages: (i) thermal equilibration of the particles (while keeping interaction of filaments and the chain negligible – to avoid hinderance of NL assembly), (ii) *deposition* of filaments close to NM, (iii) enabling interaction of the chain with the filaments, (iv) enabling *Create* and *Break* procedures for CLs and TLs, (v) reaching steady state conditions. The term *deposition* is used for when filaments have been brought within the NL region. The term *assembly* is reserved for when cross-links and transverse-links have also formed, implying a connected meshwork structure has been formed.

Step 3: The assembled NE structure will be taken through a quality check: the structure should closely represent the architecture and morphology of the mammalian NE in interphase cells. The assembly parameters will be tuned to produce this resulting coarse-grained nuclear envelope (CGNE) structure which can be used as an initial configuration for subsequent simulations and analysis.

Viscoelastic characterization

In this section, we conceptualize the framework for *in silico* mechanical testing of the CGNE for characterizing and validating its viscoelasticity with experimental estimates. We first identify which metrics of NE viscoelasticity we wish to obtain from the simulations for comparison with experiments. From applied mechanics perspective, the NE is a composite shell that can deform out-of-plane and/or in-plane. The former occurs upon bending and indentation, while the latter occurs upon stretching and shearing.

Bending elasticity: Consider the thermal fluctuation of the NM in the *resting* NE; *resting* here refers to absence of mechanical deformations such as indentation, stretching or shearing. The normal displacement of the NM particles, which is a function in spatial space, can be decomposed into a spectrum of waves/undulations of various curvatures. The elastic resistance of the NE to out-of-plane deformations can then be characterized from the fluctuation spectrum obtained from the normal displacement of the NM particles. We will obtain three metrics of bending elasticity from the fluctuation spectrum: bending modulus, B, lateral tension, Σ, and confinement stiffness, γ.

Indentation viscoelasticity: Consider next the indentation of NE with a spherical indenter of sufficiently small curvature. The out-of-plane deformation will be resisted by development of a large lateral tension in the NE, which in turn will be resisted by stretching resistance of the NE. Notwithstanding the complexity of the molecular mechanisms involved in the viscoelastic resistance of the NE to the out-of-plane deformation, such

resistance can be simply characterized from the force-depth curve recorded by the indenter. We will obtain two metrics of indentation viscoelasticity from the force-depth curves: indentation modulus, E and high-strain-rate indentation viscosity, ζ".

Stretching and shearing viscoelasticity: Consider now the stretching or shearing of NE. Again, notwithstanding the complexity of the molecular mechanisms involved in the viscoelastic resistance of the NE to the in-plane deformations, such resistance can be simply characterized from the stress-strain curves recorded from the NE deforming at a constant strain rate. We will obtain two metrics each for stretching and shearing viscoelasticity from the stress-strain curves: Young's modulus, Y and high-strain-rate extensional viscosity, ξ" in the former, and shear modulus, G and high-strain-rate shear viscosity, η" in the latter.

Dynamic viscosity: The viscosities obtained in each of the cases above were high-strain-rate viscosities. Consider finally the thermal diffusion of NPC and NL particles in the resting NE. The small-strain-rate shear viscosity in the monolayer and meshwork region of the NE can be obtained from the MSD-time curves. The small-strain-rate shear viscosity of the NE, η^* will be defined as the average value. A shear viscosity vs strain rate plot can then be made using ($\dot{\gamma}_0$, η^*), ($\dot{\gamma}_1$, $\eta"_1$), ($\dot{\gamma}_2$, $\eta"_2$) etc. We will estimate two metrics of dynamic viscosity from the shear viscosity vs strain rate plot: flow consistency index, K and flow behavior index, n.

Table 2-2 summarizes the simulation data to be collected and the theoretical models to be used to extract the metrics discussed above. The full-forms of the abbreviations used in theoretical models can be found in the List of Abbreviations.

Table 2-2 Simulation data to be collected and theoretical models to be used to obtain the metrics of NE viscoelasticity.

Simulation	**Simulation data**	**Theoretical model**	**Metrics of NE viscoelasticity**
No indentation or mechanical deformation	Fluctuation spectrum of the monolayer	CMF	B, Σ, γ
Indentation by a soft sphere	Force vs depth curve	VCM	$E, \zeta"$
Stretching deformation	Stress-strain curve	2DV	$Y, \xi"$
Shearing deformation	Stress-strain curve	2DV	$G, \eta"$
No indentation or mechanical deformation	MSD vs time of NE components	SER	η^*

Simulation Package

The simulation package, which we title as "Coarse-Grained Nuclear Envelope Simulator (CGNES)", is outlined in Figure 2-3. A copy of the simulation package is attached as a supporting material to the thesis. In a nutshell, 'initial NE' and 'initial PC' configurations (ne.data and pc.data) are generated with ne_make/ and pc_make/. Then, the NE is assembled into data/init.data via init.lmp and init.qsub. Then, NE architecture is compared with experiments in viz/. Then, NE morphology is obtained via sim.lmp, sim.qsub and commands.lmp, and compared with experiments in plt/. If the data/init.data is found to have consistent structure with the experimental data, it is considered a CGNE

structure and the data/init.restart (which is simulation state when the structure file data/init.data was exported) is used to continue towards subsequent simulations.

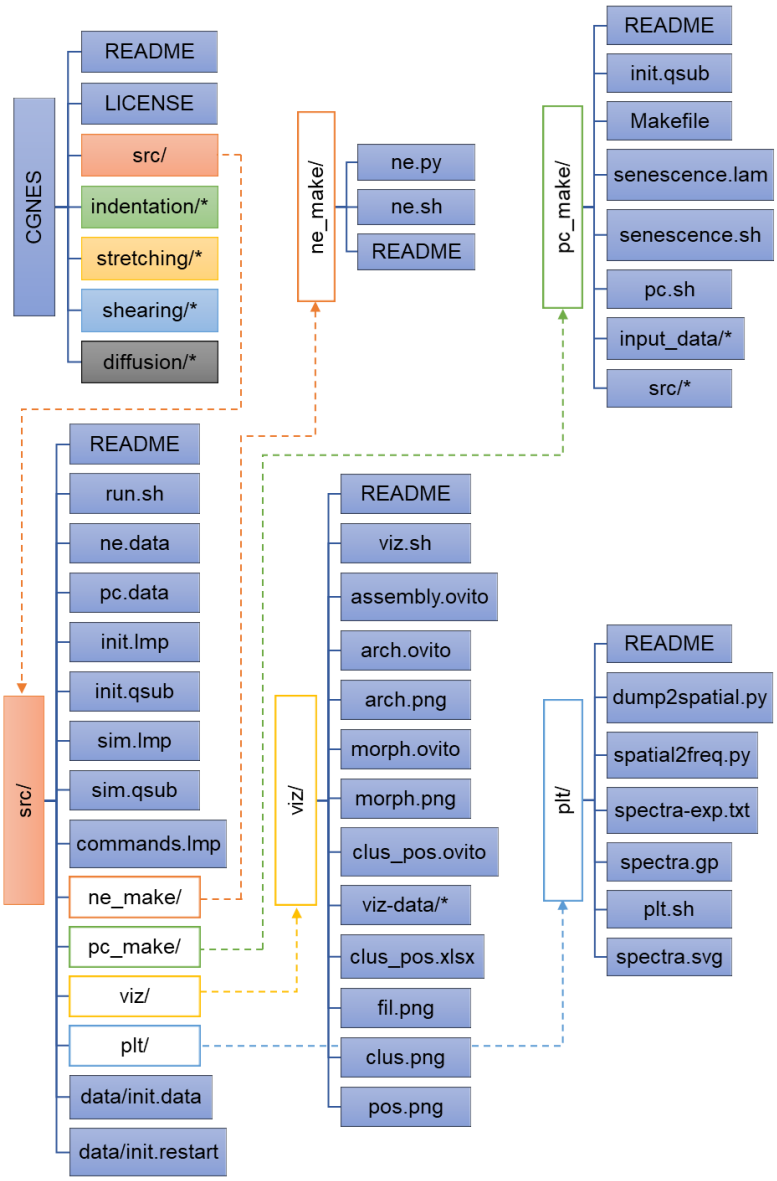

Figure 2-3 Outline of the CGNES simulation package with a few directories expanded to reveal location of files that are explicitly mentioned in the thesis. The * indicates the contents of the directory are not shown in this figure.

Chapter 3 Structure of the CGNE

In this chapter, we present a protocol that results in a CGNE structure that is representative of the architecture and morphology of the mammalian NE in interphase cells. A three-step framework was conceptualized in the fourth section of Chapter 2. In the three sections that follow, those three steps are addressed one by one.

Generating CGNE components

In this section, the procedures to generating an initial configuration of components that will comprise the three groups namely monolayer, meshwork and chain are described. On several occasions we refer to the files in the simulation package (Figure 2-3).

Monolayer and Meshwork: For the monolayer group comprising of type 1 (NM) and type 2 (NPC) particles, the positions, orientations, and shape of the particles are generated by a Python script ne.py located in src/ne_make/. For the meshwork group comprising of type 3 (NL-A) particles, type 4 (NL-B) particles, type A bonds and type A angular bonds, the positions of the particles and topology (list of particle indices) of the bonds are also generated by the same Python script. The bash script ne.sh automates the process, resulting in the 'initial NE' configuration file ne.data.

Chain: For the chain group comprising of type 5 (EC) particles, type 6 (HC) particles and type D bonds, the positions of the particles and topology (list of particle indices) of the bonds are generated by several files working together in src/pc_make/. The

bash script pc.sh automates the process and a few manual steps are described in the README. The procedure results in the 'initial PC' configuration file pc.data.

Assembling into the CGNE

In this section, the *ad hoc* CGMD simulation for assembling the CGNE components is described. The assembly is conducted via init.lmp. It reads in the configurations ne.data and pc.data and outputs data/read_data.data, data/init.dump_local, data/init.lammpstrj, data/init.data and data/init.restart. The first 3 are used to visualize the assembly (Figure 3-1). The 4th is the 'assembled NE structure', a candidate to be designated CGNE structure after comparison with experimental data in next step. The 5th is the simulation restart file to continue and run subsequent simulations for indentation, stretching, shearing and diffusion tracking of the CGNE.

Stage 1: First, the configurations ne.data and pc.data are read in, all interaction properties are assigned, all components (except PC) are minimized and data/read_data.data is exported for use as structure file in assembly.ovito. The configuration of the monolayer as a flat layer of two types of particles, that of the 'meshwork' as vertically grown filaments of two types, and that of the chain as a random walk with two types of beads can be seen in the top left panel in Figure 3-1.

Stage 2: Next, thermal equilibration of the particles is performed with a few settings introduced, either permanently or temporarily, in between. The following settings

are introduced before the simulation commences: (i) interaction of filaments and the chain is made temporarily negligible to avoid hinderance of NL assembly, (ii) the COM of the monolayer is fixed to avoid drifting due to random forces from solvent and also from the impact of NL filaments during the forced deposition in next stage, (iii) reflective walls are placed to implement reflective boundary conditions, (iv) the velocities are initialized (approximately) with the target temperature, and (v) the Nose-Hoover thermostat is enabled to seek thermal equilibration. The following settings are introduced during the simulation: (i) if any PC chain bonds were overstretched during simulation box rescaling, they are relaxed, (ii) if any NPCs were accidently generated next to each other, they are pushed away gradually, and (iii) the Nose-Hoover thermostat is replaced with the Langevin thermostat, although with a temporarily low viscosity. The thermally excited configuration of monolayer particles and meshwork filaments can be seen in the top right panel in Figure 3-1. The temporarily large undulations of the monolayer are expected due to the imbalance of partition of the translational and rotational energy prior to equilibration.

Step 3: Next, deposition of meshwork beneath the monolayer is performed, with preference to NL-B, using temporary purely repulsive walls. Once NL is sufficiently close to the monolayer, a reflective wall is placed temporarily. The deposited NL can be seen in the middle left panel in Figure 3-1.

Step 4: Next, interaction of filaments and the chain is enabled (interaction strength increased from negligible value set earlier) and the repulsive walls used for deposition are

removed. While these changes are not visualized, the absence of links is visualized in the middle right panel in Figure 3-1.

Step 5: Next, the CLs and TLs are enabled along with gradual increase of the damping. Newly formed CLs are visualized in the bottom left panel in Figure 3-1.

Step 6: Finally, the ad hoc assembly simulation is transitioned to simulation conditions. The following are done as a part of this process: (i) reflective wall that was used to hold deposited NL is removed, (ii) if any particle is under more than 100 pN force, the particle's, and accordingly neighboring particles', position(s) are directly adjusted, (iii) increase the damping to the value to be used in subsequent simulations. Finally, we let the simulation run for a while to ensure steady state conditions are reached. The use of step (ii) may not be obvious and indeed an optional trick. The idea is to heavily reduce time needed in reaching steady state by quickly adjusting unstable particles in advance instead of waiting for them to adjust on their own in the highly damped environment. Note that we use this step only to bring the closer to an equilibrium state and not as a proxy for equilibration by integrating equations of motion. The simulation is allowed to run for sufficient duration to reach an equilibrium state. Part of the process in the next section is a subsequent simulation instructed by commands.lmp (which is run via sim.lmp and sim.qsub). Before extracting the NE morphology, additional commands in commands.lmp collect time-series of temperature of various CGNE components, various energies, and various stresses in the CGNE into data/equil.txt. Fluctuation of all of these quantities within

10% about an average value during 1 million timesteps confirmed that the state is sufficiently stable on the timescales on the simulation.

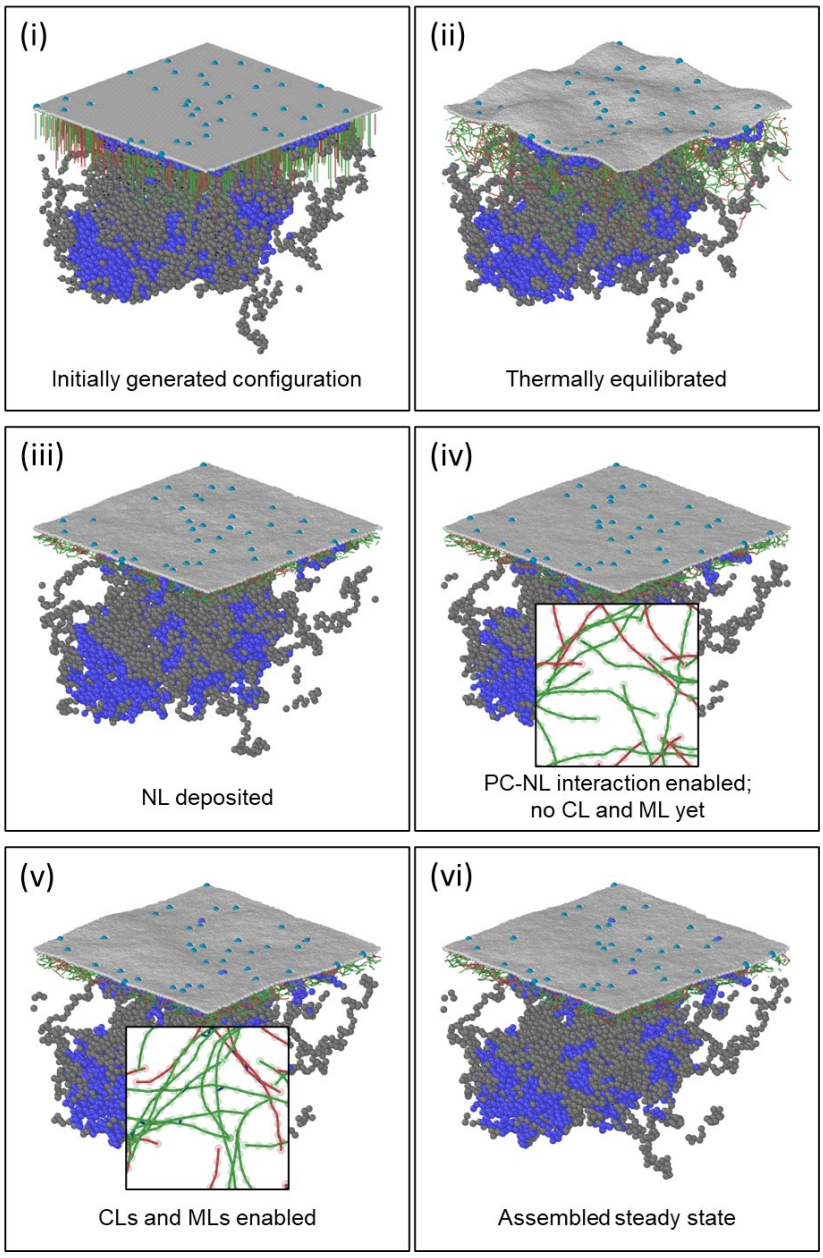

Figure 3-1 Snapshots of the NE assembly via *ad hoc* CGMD simulation. The six snapshots (i) to (vi) correspond to the six stages. The square-shaped NE patch is $2.5\ \mu m \times 2.5\ \mu m$ in size.

Validation with experimental data

In this section, the procedure of comparison of the assembled NE structure with experimental data on the architecture and morphology of the mammalian NE in interphase cells is described.

In an early stage of the project, shallow validation of basic aspects of the NE structure to achieve visual similarity in experiments and simulations was performed due to limited availability of experimental data. However, a thorough validation of compositional and structural properties became possible in the late stages as new experimental data emerged. The additional quality control imposed by the procedure described here is expected to improve the predictive capabilities of the model. Indeed, viscoelastic properties of polymers are strongly influenced by structural features such as degree distribution of network connectivity (Sapra et al. 2020), polydispersity (Struglinski and Graessley 1985), molecular weight (Doi and Edwards 1988), and concentration (Doi and Edwards 1988). Similar is the situation with membranes whereby composition affects viscosity and bending rigidity (Steinkühler et al. 2019).

Basic comparison: Before the detailed structural comparison that follows, a basic comparison of structural properties that can be readily compared is presented in Table 3-1. Most values could be used (or achieved by parameter tuning) close to experimental data. The NM thickness was calculated as the equilibrium separation for the NM and NL particles. The NM pore diameter was calculated visually as the average diameter of hole in NM. While the thickness of the assembled NL depends on several factors such as mutations

and stiffness of the ECM (Joe Swift et al. 2013), full width at half maximum (FWHM) method was used to infer NL thickness from Figure 3-2d; the same method has been used to obtain this quantity from experimental data (Nmezi et al. 2019; Turgay et al. 2017). Lateral separation of globular domains in experiments was used as the experimental estimate of NL filament thickness, instead of the thickness of the rod domain, which was 3.5 nm (Turgay et al. 2017). The NL filament thickness in CGNE was correspondingly calculated as the equilibrium separation for the NL particles since the NL particles coarse-grain the globular domains.

Table 3-1 Comparison of estimates of structural properties in experiments and values used (or achieved) in CGNE structure.

Property	**Experimental data**	**CGNE**
NM thickness	50 nm (Beck et al. 2007)	50 nm
NM pores per unit area	6 μm^{-2} (Turgay et al. 2017)	6 μm^{-2}
NM pore diameter	70 nm (Beck et al. 2007)	70 nm
NL thickness	80 nm (Nmezi et al. 2019)	70 nm
NL filaments per unit area	207 μm^{-2} (Turgay et al. 2017)	207 μm^{-2}
NL filament thickness	12 nm (Turgay et al. 2017)	12 nm
NL filament length, average	380 nm (Turgay et al. 2017)	380 nm

NE architecture: Visually, the overall architecture of the NL in the CGNE and experiments is very similar (Figure 3-2a). The oligomeric assembly of lamin filaments involves lateral and longitudinal associations of dimerized lamins resulting in a highly polydisperse meshwork i.e., the filament lengths are highly variable (Turgay et al. 2017). While generating the NL filaments, we used this experimental filament length distribution. Hence, the fraction of filament of certain lengths in the CGNE structure and experiments

is almost the same (Figure 3-2b); the small differences being due to rounding-off of filament length to multiples of 20 nm, the bond length for type A bonds. The fraction of network node degree in experiments and CL cluster size in the CGNE structure have a similar power-law distribution (Figure 3-2c). The stacking of the NM, NL-B, NL-A and PC as observed in experiments (Nmezi et al. 2019; Turgay et al. 2017) is also comparable (Figure 3-2d), although better assembly parameters could have been chosen to achieve NL-B closer to the NM. A lamin-A:B stoichiometry of 2 i.e. twice as many NL-A than NL-B was used (Figure 3-2a), which is at the middle of the proteomics map of lamin-A:B stoichiometry versus tissue microelasticity (Joe Swift et al. 2013).

NE morphology: The z-displacement of the particles of the NM was decomposed into a fluctuation spectrum (Figure 3-3). The fluctuation spectrum is very informative as it informs about the amplitude of undulations of various wavelengths that develop on a membrane due to thermal fluctuations. Figure 3-3a shows morphology of the NM in the CGNE by color coding the particles with their z-displacement. The z-displacement is renamed as 'Membrane deformation' for a more intuitive presentation of the sub-figure. Consider that u_i is the z-displacement of the i^{th} NM particle. Since each particle has an associated position in the xy-plane described by (x_i, y_i), let $u_{x,y}$ be a function that returns the z-displacement, u_i for a list of nonuniform grid points (x_i, y_i). Using 2D nonuniform fast Fourier transform, we converted $u_{x,y}$ to u_{q_x,q_y}, where q_x and q_y are the wavenumbers in x and y directions. The time-averaged fluctuation spectrum, $\langle u^2_{q_x,q_y} \rangle$ was obtained from 10 snapshots. This 2D fluctuation spectrum was radially averaged to obtain the 1D

fluctuation spectrum $\langle u_q^2 \rangle$ vs q which is plotted in Figure 3-3b. The fitting with CMF theoretical model to obtain metrics of bending elasticity will be discussed in next chapter.

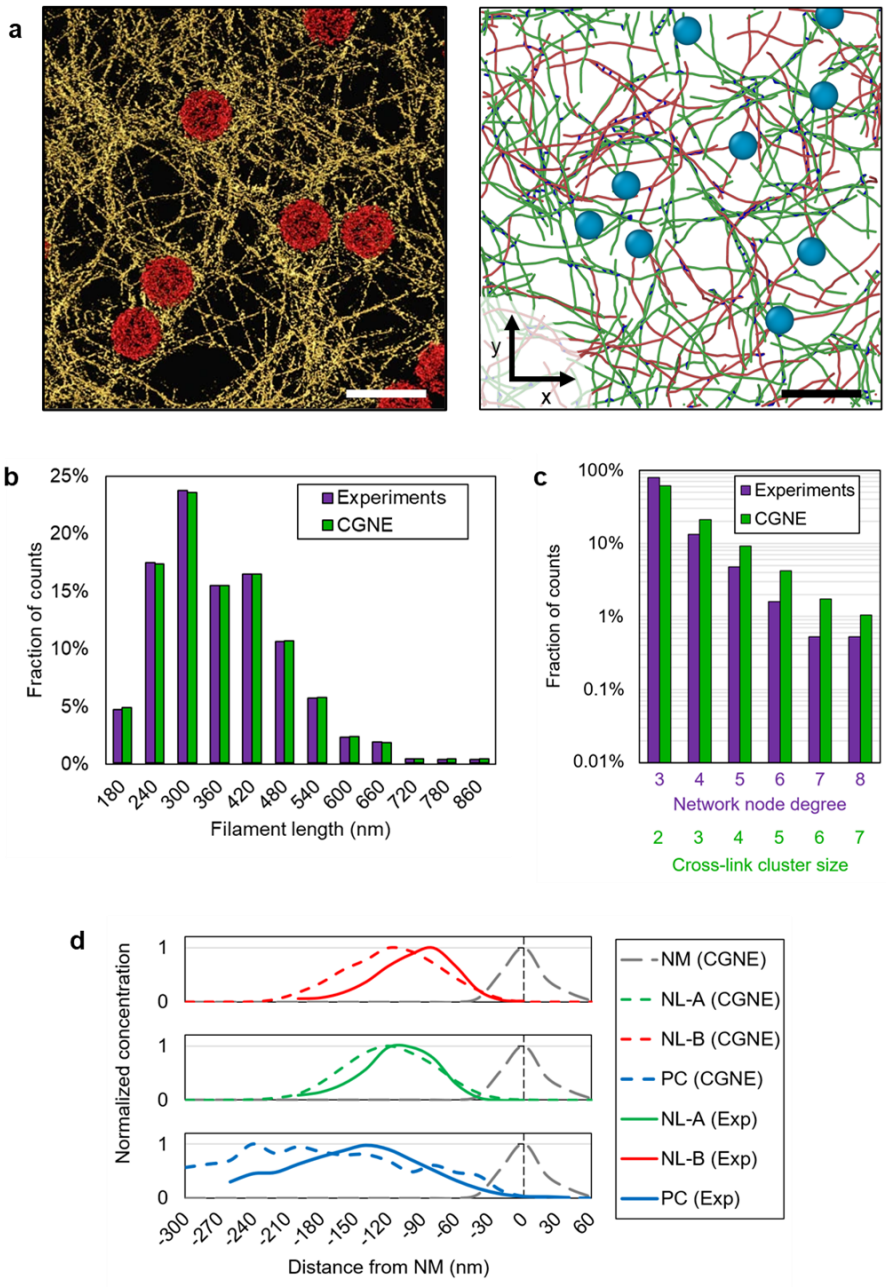

Figure 3-2 Architecture of the NE in experiments and simulations. **a**, Structure of NL in experiments (left) and CGNE (right). Scale bar: 200 nm. **b and c**, Quantitative comparison

of the in-plane (xy) architecture of NL in experiments vs CGNE via histograms of the relative frequency distribution of filament length (**b**) and meshwork connectivity (**c**). In experiments, variability of meshwork connectivity was quantified with node degree in an undirected graph of NL e.g., 5 lamin filaments emanate from a node of degree 5. In simulations, the variability was similarly quantified with cluster size of cross-links e.g., 5 lamins are cross-linked in a cluster of size 5. **d**, Quantitative comparison of the out-of-plane (z-axis) architecture of NE components via distribution of position of particles with respect to NM. Source of the experimental image in **a** is (Turgay et al. 2017). Sources of experimental data are: data in **b, c and d** were obtained from (Turgay et al. 2017), (Sapra et al. 2020), and (Nmezi et al. 2019).

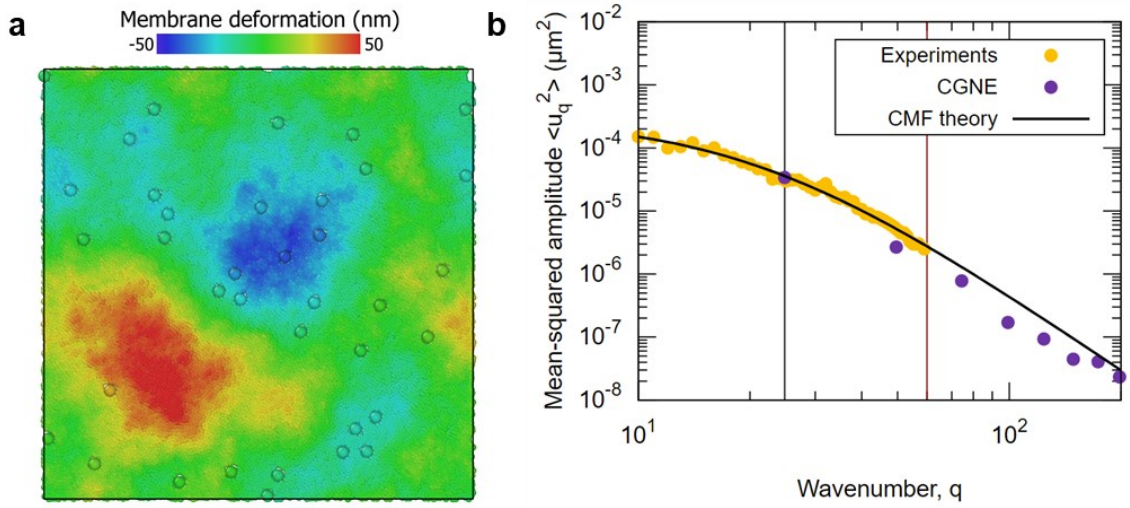

Figure 3-3 Morphology of the NE in experiments and simulations. **a**, The z-displacement of monolayer particles in the CGNE. **b**, Comparison of fluctuation spectrum in experiments (yellow) and CGNE (magenta). The CMF theory (black) was also used to fit the experimental and simulation data for obtaining three metrics of bending elasticity of the NE: bending modulus, B, lateral tension, Σ, and confinement stiffness, γ. Source of experimental data in b: (Chu, Haley, and Zidovska 2017).

Chapter 4 Viscoelasticity of the CGNE

In this chapter, we present methodologies for *in silico* mechanical testing of the CGNE and extraction of metrics of NE viscoelasticity from the simulation data. The tests are: membrane flickering spectroscopy, indentation, stretching, shearing and diffusion tracking of the CGNE. The tests characterize bending elasticity, indentation viscoelasticity, stretching viscoelasticity, shearing viscoelasticity, and dynamic viscosity of the CGNE, respectively. As described in the fifth section of Chapter 2, the characterization will be done by fitting the simulation data for various metrics of NE viscoelasticity. As noted in the fourth section of Chapter 1, we present only the methodology but exclude the results – as they are not publication ready. In the last section, we describe the visualization modules with which simulation results are double-checked for any unexpected structural change. This is especially important with the ongoing parameter tuning.

Bending elasticity

Assembled as a shell encapsulating the interphase chromatin, a key duty of the NE is to resist indentation from foreign bodies which can cause bending of the NE. Experimental studies have shown that large curvatures highly reduce NL density (Nmezi et al. 2019) – which may break peripheral nuclear structures such as LADs and affect transcription activity as a result (Ulianov et al. 2019), and extreme curvatures rupture entire NE leading to potential loss of DNA repair factors (Xia et al. 2018). Computational investigation of integrity of membrane-lamina-chromatin connections relevant to such phenomena remains precluded by the lack of a computational model that features these

connections and its simulation is physiologically relevant. With the capability of our CGNE model in meeting the former requirement demonstrated, we proceed to characterize its bending elasticity.

A classical approach in assessing inherent bending resistance of membranes without introduction of a foreign body as a probe, is to decompose the surface morphology of membrane, fluctuating under thermal noise, into a fluctuation spectrum (Brandt et al. 2011). In this approach, the bending modulus B and lateral tension Σ of biomembranes such as lipid bilayers are obtained by fitting the fluctuation spectra $\langle u_k^2 \rangle$ vs angular wavenumber k using the following relationship from Helfrich elastic membrane theory (Brandt et al. 2011):

$$L^2 \langle u_k^2 \rangle = \frac{k_B T}{(Bk^4 + \Sigma k^2)}$$

where, $k = \frac{2\pi}{\lambda}$, λ is the wavelength of membrane undulations, and $L = L_x = L_y$ is length of the sides of the square patch of the membrane.

However, care must be taken while using homogenized theoretical models to obtain biophysical properties of a composite: the NE is not just a membrane but a membrane (NM) associated with a cortical layer (NL). Applying this approach directly to fit experimental data in Figure 3-3b gave $B = 32\ k_B T$ and $\Sigma = 0.0144\ mN/m$. While single lipid bilayers can sustain up to about $12\ mN/m$ lateral tension (Boucher et al. 2007), the stiff NL in bone cells cannot sustain more than $0.016\ mN/m$ of lateral tension (Deviri et al. 2019); the value is calculated as $\Sigma_{critical} = t_{NL} E \varepsilon_{critical}$, where $t_{NL} = 80\ nm$ is the thickness of NL,

$E = 0.2kPa$ is the Young's modulus of NL, and $\varepsilon_{critical} = 1.12$ is the disassembly strain. In fact, the experimental data comes from HeLa cells (Chu, Haley, and Zidovska 2017), which have a similar stiffness as A549 cells and are therefore expected to have about half the NL than bone cells (Joe Swift et al. 2013).

Interestingly, such issue of high membrane tension from theoretical fitting was also reported for red blood cells, and a composite membrane fluctuation (CMF) theory was developed (Gov, Zilman, and Safran 2003). The modified theory incorporates the role of an underlying protein layer with a simple additional term in denominator compared to the original equation:

$$L^2\langle u_k^2\rangle = \frac{k_B T}{(Bk^4 + \Sigma k^2 + \gamma)}$$

where, γ is the confinement stiffness of the protein layer. Fitting with this equation gave $B = 32\ k_B T$, $\Sigma = 0.0074\ mN/m$ and $\gamma = 11 \times 10^6\ N/m^3$. These values are close to those estimated for red blood cells: $B = 7\ k_B T$, $\Sigma = 0.005\ mN/m$ and $\gamma = 4 \times 10^7 N/m^3$ (Gov, Zilman, and Safran 2003), which is quite surprising. The larger bending modulus for NE is expected since the NM is actually two bilayers, and the NL filaments have an order of magnitude larger persistence length of about 500 nm than spectrin tetramers with about 10 nm (Lai et al. 2015).

Hence, three metrics of NE bending resistance namely the bending modulus, B, lateral tension, Σ and confinement stiffness, γ were obtained from the theoretical fit in Figure 3-3b. Note that the plot is $\langle u_q^2\rangle$ vs q and not $\langle u_k^2\rangle$ vs k. The wavenumber $q = \frac{L_c}{\lambda}$ in

experiments (with entire nucleus of contour length $L_c \approx 62\ \mu m$) is related to $k = \frac{2\pi}{\lambda}$ in simulations (with a patch of NE) via $k = \frac{2\pi}{L_c} q$. The theoretical equation for fluctuation spectrum i.e., mean-squared wave amplitude $\langle u_q^2 \rangle$ vs wavenumber, q is therefore:

$$\langle u_q^2 \rangle = \frac{L_c^2}{16\,\pi^4\,\frac{B}{k_B T}\left(\frac{L}{L_c}\right)^2 q^4 + 4\,\pi^2\,\frac{\Sigma}{\frac{k_B T}{\tilde{\sigma}^2}}\left(\frac{L}{\tilde{\sigma}}\right)^2 q^2 + \frac{\gamma}{\frac{k_B T}{\tilde{\sigma}^4}}\left(\frac{L}{\tilde{\sigma}}\right)^2\left(\frac{L_c}{\tilde{\sigma}}\right)^2}$$

where, $L_c = 62\ \mu m$ is the contour length of the nucleus in experiments, $L = 2.5\ \mu m$ is the length of sides of the square patch of NE in simulations, $\tilde{\sigma} = 10\ nm$ is the simulation length scale, $k_B = 1.380649 \times 10^{-23} J/K$ is the Boltzmann constant, and $T = 300\ K$ is the temperature. This is the equation used in src/plt/spectra.gp to plot 'CMF theory'.

Clearly, it is straightforward to obtain the values of B, Σ and γ for the CGNE by simply fitting with the data points 'CGNE' in Figure 3-3b with the same equation. However, as noted earlier in fourth section of Chapter 1, we do not present this result here since the values may be significantly different when we finish tuning the parameters.

Indentation viscoelasticity

In addition to the bending elasticity metrics obtained under no perturbation from a foreign body (note the absence of cytoskeletal structures such as F-actin and microtubules in our model), we can also estimate resistance of CGNE to indentation against a soft spherical indenter representing a coarse-grained foreign body. The indenter will act as a

displacement-controlled force probe. Based on fundamental concepts in viscoelasticity and contact mechanics, we derive below equations to obtain the indentation modulus, E and indentation viscosity, ζ" from the force-depth curves as metrics of indentation viscoelasticity.

Indentation of the NE can be considered as indentation of a viscoelastic half space whereby the total force, F on the indenter is a superposition of the elastic, F_{el} and viscous, F_{visc} resistive forces. A classical result in contact mechanics was derived by Heinrich Hertz relating the elastic contact load, F_{el} and load-point displacement, d for the contact of an elastic sphere, of radius R', elastic modulus E' and Poisson's ratio, ν', with the surface of an elastic specimen of elastic modulus E and Poisson's ratio, ν (Fischer-Cripps 2007):

$$F_{el} = \frac{4}{3} E_c R'^{1/2} d^{3/2}$$

where, E_c is the contact modulus given by $\frac{1}{E_c} = \frac{1-\nu^2}{E} + \frac{1-\nu'^2}{E'}$. We derived the equation of F_{visc} as below.

The superimposed contact stress in the contact region can be written in a Kelvin-Voigt representation of a spring and dashpot in parallel: $\sigma_c = \sigma_{el} + \sigma_{visc}$, where $\sigma_{el} = E_c \epsilon$ and $\sigma_{visc} = \zeta_c \dot{\epsilon}$ for the contact viscosity ζ_c and contact strain ϵ_c. The radius of contact derived by Hertz was $a = \sqrt{R'd}$. Using $F_{el} = \sigma_{el} \pi a^2$, $\epsilon = \frac{4}{3\pi}\sqrt{\frac{d}{R'}}$. Hence, $\dot{\epsilon} = \frac{2}{3\pi}\frac{\dot{d}}{\sqrt{R'd}}$. Using $F_{visc} = \sigma_{visc} \pi a^2$, we obtain:

$$F_{visc} = \frac{2}{3} \zeta_c R'^{1/2} d^{1/2} \dot{d}$$

Hence, the total force on the indenter is given by $F = \left(\frac{4}{3}E_c R'^{\frac{1}{2}}\right) d^{3/2} + \left(\frac{2}{3}\zeta_c R'^{\frac{1}{2}}\dot{d}\right) d^{1/2}$.

Using an elastic sphere of fixed/same radius R', the CGNE can be indented at three speeds of $\dot{d}_1 = \dot{d}_2/3$, $\dot{d}_2$ and $\dot{d}_3 = 3\,\dot{d}_2$ and the force on the indenter F_1, F_2 and F_3 recorded. If $\dot{d}_2 = 27\,mm/s$ is used, these speeds are about 900 times faster than indentation speeds in experiments for an approximately $100\,nm$ wide tip (Wang et al. 2018). To avoid puncturing the NE at such high indentation speed, we used $R' = 1\,\mu m$ i.e., ten times larger indenter which allowed a deformation of the monolayer without puncturing over indenter travel distance of 100 nm. We now describe the procedure and assumptions under which E and ζ" can be obtained from the force-depth curves.

Considering the indenter is not viscoelastic, we can assume that the contact viscosity, ζ_c registered by the indenter is the indentation viscosity ζ". Hence ζ" will be obtained by fitting the difference of force in first and third indentation speeds according to:

$$\Delta F_{31} = F_3 - F_1 = \left(\frac{2}{3}\zeta_c R'^{\frac{1}{2}}(\dot{d}_3 - \dot{d}_1)\right) d^{1/2}$$

Now, if the indenter spring constant $K \to \infty$, indenter modulus $E' \to \infty$ and thereby $E \to E_c\,(1-\nu^2)$. Therefore, the indentation modulus, E can be obtained as $E \approx \frac{3}{4}E_c$ by using a large value of K, and assuming $\nu = 0.5$. Hence, once $\zeta" = \zeta_c$ is obtained as

described above, E will be obtained by fitting the difference of force for the second indentation speed and expected viscous force according to:

$$F_{el,2} = F_2 - \left(\frac{2}{3}\zeta" R'^{\frac{1}{2}} \dot{d}_2\right) d^{1/2} = \left(\frac{16}{9} E R'^{\frac{1}{2}}\right) d^{3/2}$$

The experimental estimates of indentation modulus, E and indentation viscosity, $\zeta"$ found in literature are: $E = 0.25\ to\ 2\ kPa$ for indenter tip radius ranging from infinite to about 100 nm (Wang et al. 2018; Wei et al. 2016), and $\zeta" = 1 \times 10^6\ cP$ (Wang et al. 2018). The cell types used in these experiments (T24 and RT4 in (Wang et al. 2018) and HEK-293 and L929 in (Wei et al. 2016)) indeed belong to the lower tissue microelasticity group (0.1-1 kPa) and scaling of NL is therefore not necessary for comparison (Joe Swift et al. 2013).

Clearly, it is straightforward now to obtain the values of E and $\zeta"$ for the CGNE: ΔF_{31} and $F_{el,2}$ are fitted after obtaining the F vs d for the 3 indentation speeds with the code implemented in indentation/* (Figure 2-3). However, as noted earlier in fourth section of Chapter 1, we do not present this result here since the values may be significantly different when we finish tuning the parameters.

In-plane viscoelasticity

While the cytoplasm of migrating cells easily penetrates sub-micron pores, the nucleus bottlenecks the migration (Denais et al. 2016). The increase of NE curvature in

nuclei squeezing through tight spaces can lead to NE rupture (Shah, Wolf, and Lammerding 2017). Bending resistance of the NE, which limits curvature of NE, can therefore limit migration through narrow constrictions. However, when a constriction is large, the NE of migrating nucleus may not incur curvature large enough to trigger NE rupture. Instead, the NE may stretch with a possibility of NL rupture (Deviri et al. 2019). In this scenario, NE blebbing occurs and chromatin flows into the bleb. The bleb, smaller than the nucleus and with reduced amount of NL (Deviri et al. 2019), is susceptible to NE rupture. Therefore, high stretching resistance of NE might be important in protect it from eventual rupture in such conditions. High shearing resistance of NE will limit distortions of the NE, which could disrupt NL and/or LADs. Hence, we characterize the stretching and shearing viscoelasticity of the CGNE, i.e., its resistance to in-plane deformation and flow, by recording evolution of stress vs strain under a constant strain rate. We use the two-dimensional viscoelasticity theory to obtain the Young's modulus, Y, high-strain-rate extensional viscosity, $\xi"$, shear modulus, G and high-strain-rate shear viscosity, $\eta"$ as metrics of in-plane viscoelasticity.

The NE in the CGNE can be considered as a composite shell under a state of plane stress – as cytoskeletal structures that may induce stress in the normal direction are not included in the model. The composite material of the NE can be assumed to be isotropic, due to random alignment of filaments and the chain, and viscoelastic, due to presence of viscous dissipation and reversible linking mechanisms. The equation relating the elastic

stresses and small stretching and shearing deformations, can be formulated using 2D linear elasticity as $\sigma_x^{el} = \frac{Y}{1-\nu^2}(\varepsilon_x + \nu\varepsilon_y)$, $\sigma_y^{el} = \frac{Y}{1-\nu^2}(\varepsilon_y + \nu\varepsilon_x)$ and $\tau_{xy}^{el} = G\gamma_{xy}$.

First consider stretching. We will stretch the NE in x-direction at a constant strain rate of $\dot{\varepsilon}_x = 1.08 \times 10^4\ s^{-1}$ (elongates NE in x-direction at $27\ mm/s$) while maintaining a constant NE patch area, $A = L_x L_y$ by compressing in y-direction according to $\dot{\varepsilon}_y = -\dot{\varepsilon}_x \frac{1+\varepsilon_y}{1+\varepsilon_x}$. The reflective boundaries in the z-direction will be held fixed. Constant area stretching has the advantage of allowing large deformation without challenging the incompressibility of the monolayer. Lipid bilayers fracture at about 5-10% areal strain. It is also a better choice than the mixed boundary condition of maintaining the stress in lateral direction constant, σ_y^{el} since in that case the strain rate would need to be extremely low to ensure the NE contracts in y-direction sufficiently quickly to avoid areal strain reaching close to causing monolayer fracture. Integrating the equation for $\dot{\varepsilon}_y$ and using $\varepsilon_y = 0$ for $\varepsilon_x = 0$ to eliminate constant of integration, we have $\varepsilon_y = -\frac{\varepsilon_x}{1+\varepsilon_x}$. Since the maximum strain up to which the NE will be stretched is much smaller than 1 ($\varepsilon_{x,max} = 0.05$), we can approximate ε_y as $-\varepsilon_x$. Hence, the elastic tensile stress in x-direction becomes: $\sigma_x^{el} = \frac{Y}{1+\nu}\varepsilon_x$.

We also consider shearing of the NE at a constant strain rate of $\dot{\gamma}_{xy} = 1.08 \times 10^4\ s^{-1}$. Simple shear will be applied, which maintains a constant NE patch area automatically. The elastic shear stress in the xy-plane remains the same: $\tau_{xy}^{el} = G\gamma_{xy}$.

We have used the superscript "el" so far to indicate the elastic stresses. As the material deformed states are achieved through continuous deformation under constant strain rate, viscous stresses $\sigma_x^{visc} = \xi"\dot{\varepsilon}_x$ and $\tau_{xy}^{visc} = \eta"\dot{\gamma}_{xy}$ will arise. These can be considered superimposed with the elastic stress according to a Kelvin-Voigt representation of the viscoelastic behavior as a spring and dashpot in parallel: $\sigma_x = \sigma_x^{el} + \sigma_x^{visc}$ and $\tau_{xy} = \tau_{xy}^{el} + \tau_{xy}^{visc}$.

The 1st equation will be used to fit the stress-strain behavior under stretching to obtain the slope $\frac{Y}{1+\nu}$, from which the Young's modulus will be deduced assuming $\nu = 0.5$, and intercept $\xi"\dot{\varepsilon}_x$, from which the extensional viscosity, $\xi"$ will be obtained. The 2nd equation will be used for stress-strain behavior under shearing to obtain the shear modulus, G as the slope and high-strain-rate shear viscosity, $\eta"$ as the intercept divided by $\dot{\gamma}_{xy}$.

We describe now how the NE stresses were estimated. For a collection of M particles in a sub-volume of size $s_x \times s_y \times s_z$, the stress tensor $\boldsymbol{\sigma}$ is given by:

$$\boldsymbol{\sigma} = \frac{1}{V}\left(-\sum_{i}^{M} m_i \boldsymbol{v}_i \otimes \boldsymbol{v}_i - \frac{1}{2}\sum_{i}^{M}\sum_{j(\neq i)}^{M} \boldsymbol{r}_{ij} \otimes \boldsymbol{F}_{ij} \right)$$

where, $\boldsymbol{r}_{ij} = \boldsymbol{r}_i - \boldsymbol{r}_j$, $V = s_x s_y s_z$ and $\boldsymbol{F}_{ij}$ is the force exerted on particle i by particle j. While a small cluster of particles may diffuse and mix in various sub-volumes of the simulation box, the periodic boundary conditions in x- and y- direction and the reflective boundary conditions in z-direction ensure that the collection of all particles is

confined to the simulation box region of $L_x \times L_y \times L_z$ over the entire simulation. We therefore selected the entire simulation box region as the sub-volume of interest and obtained $\boldsymbol{\sigma}^{box}$ for the collection of NE particles, i.e., type 1 to 4. The NE stresses, σ_x and τ_{xy} can be obtained from the stress tensor of simulation box, $\boldsymbol{\sigma}^{box}$ via: $\sigma_x = \frac{L_z}{t_{NE}}\sigma_x^{box}$ and $\tau_{xy} = \frac{L_z}{t_{NE}}\tau_{xy}^{box}$, where t_{NE} is the thickness of the NE. Since NL has a porous structure, with filaments binding and unbinding in and out of the NL, the lower surface of the NE is rough and uneven. A common approach to estimate thickness of such structures is to take the FWHM from the z-distribution of density of particles. For example, the NL thickness in experiments will be obtained with this approach. An alternative approach to obtain NE stress is to select the region covered by FWHM as the sub-volume. In this case, the sub-volume is well defined. However, due to the shuffling of particles in and out of the sub-volume, the validity of the stress tensor equation above may be compromised (Zhou 2003). In conclusion, our calculation of 'NE stresses' is an estimate as good or as bad as any other estimate due to the porous structure of the NL. However, provided that we use a consistent method to obtain them, they can be, in principle, used for comparative analyses within our work e.g., to assess the change of in-plane viscoelasticity upon change of lamin-A:B stoichiometry.

The experimental estimates of in-plane viscoelasticity metrics found in literature are: $Y\ and\ G$ in the range of $0.5 \pm 0.4\ kPa$ under combined shearing and stretching as observed in micropipette aspiration (Joe Swift et al. 2013; Wintner et al. 2020). Estimates

of ξ" and η" have not been found. Instead, the low-strain-rate shear viscosity, η^* has been reported in the range of $5 \pm 3 \times 10^6\ cP$ (Joe Swift et al. 2013; Wintner et al. 2020).

Clearly, it is straightforward now to obtain the values of Y, G, ξ" and η" for the CGNE via the above procedure which has been implemented in stretching/* and shearing/* (Figure 2-3). However, as noted earlier in fourth section of Chapter 1, we do not present this result here since the values may be significantly different when we finish tuning the parameters.

Dynamic viscosity

Viscosity - the resistance to flow - of a material has a distinct significance to its elasticity - resistance to deformation. The significance of elastic resistance of NE is that it limits large deformations under a given stress. However, even a small stress, if prolonged for a long time, can result in a large deformation due to nanoscale material flow. The nanoscale mechanism of viscous flow of NE has been a subject of detailed experimental investigation with important insights (Dahl et al. 2005) (J. Swift and Discher 2014) (Stephens et al. 2017) (Wintner et al. 2020). While these studies obtained insights on the distinct role of NE components in the flow resistance (viscosity) of the entire NE, the mechanistic details remain unclear.

In rheology, the shear viscosity estimated at low-strain-rate, η^* and that obtained at high-strain-rate, η" can be orders of magnitude different indicating strain-rate dependence.

Such 'dynamic' viscosity, η can be described with a Power-law rheology model defined as:

$$\eta = K(\dot{\gamma})^{n-1}$$

where, K is the flow consistency index and n is flow behavior index. These material parameters can be obtained by linear regression fitting of $\log(\eta)$ vs $\log(\dot{\gamma})$ for different strain rates. However, before doing so, the low-strain-rate shear viscosity η^* needs to be determined. The process of doing so is described below.

The mean squared displacement (MSD) of a self-diffusing (thermally driven) particle in a viscous medium is given by:

$$MSD(t) \approx 2n_{dim}\, D\, t$$

where, D is the diffusion coefficient, n_{dim} is dimensions of motion and t is the time. Using the above relationship, the diffusion coefficient D can be obtained. Also, if the hydrodynamic diameter, d of the particle is known, the Stokes-Einstein Relation (SER), $D \approx \frac{k_B T}{\gamma} = \frac{k_B T}{3\pi\eta^* d}$ can be used to obtain the low-strain-rate shear viscosity of the medium, η^* as experienced by the particle can be deduced.

Experiments on entangled semiflexible polymers (viscoelastic media) have established the following regarding MSD vs time (Doi and Edwards 1988):

a) The MSD of self-diffusing particles on polymeric chains do obey the relationship $MSD(t) \approx 2n_{dim}\, D\, t$, but only at small- and long-time scales.

Hence, $MSD(t) \approx \begin{cases} 2n_{dim}\, D_s\, t & t < t_s \\ 2n_{dim}\, D_l\, t & t > t_l \end{cases}$. Where, s corresponds to the small scale and l corresponds to the long scale.

b) The Diffusion coefficient in these two regimes should be separately obtained since the viscous dissipation mechanism is different. At small scales, the solvent contributes to viscous dissipation of the particle. Hence, $D_s \approx \frac{k_B T}{\gamma_{sol}} = \frac{k_B T}{3\pi\eta^*_{sol} d}$. While, at long scales, entanglements in the meshwork contribute to the friction. Hence, $D_l \approx \frac{k_B T}{\gamma_{mesh}} = \frac{k_B T}{3\pi\eta^*_{mesh} d}$.

Based on these observations, we expect to deduce η^*_{mesh} as the viscosity of the meshwork region of the NE by fitting $MSD(t) = 2n_{dim}\ \frac{k_B T}{3\pi\eta^*_{mesh} d}\ t$ in the long-timescale. The monolayer is not polymeric and therefore we expect $MSD(t) \approx 2n_{dim}\ \frac{k_B T}{3\pi\eta^*_{mono} d}\ t$, from which η^*_{mono} will be deduced as the viscosity in the monolayer region of the NE.

We collect the mean-squared displacement (MSD) vs time of NPC particles (which represent individual 100 nm wide nuclear pore complexes), NL-A and NL-B particles (which represent 14 nm wide globular domains on nuclear filaments), and HC and EC particles (which represent 70 nm wide mesoscale domains of chromatin), and obtained the shear viscosity, η^* experienced by the NE components located in the membrane and meshwork region. The theoretical equation for MSD, $\langle r^2 \rangle$ vs time, t is given by:

$$\langle r^2 \rangle = 2n_{dim}\ \frac{k_B T}{3\pi\eta^* d}\ t$$

where, n_{dim} is the dimensions of motion of the tracked particle (2 for NPC in the monolayer and 3 for NL-A and NL-B in the meshwork) and d is the hydrodynamic diameter of the tracked particle. We will skip tracking NM particles as the NPC already provide estimate of viscosity in the monolayer region. The NL-A and NL-B provide estimate of viscosity in the meshwork region. While of same hydrodynamic sizes, both of these components of NL will be tracked since they have different types of interactions in the NE. The MSD of EC and HC will also be tracked as they interact with the NE despite not being a part of it. The component-specific viscosities will be averaged to obtain the composite viscosity, η^* of the NE.

Clearly, it is straightforward now to obtain the value of η^* for the CGNE via the above procedure which has been implemented in diffusion/* (Figure 2-3). However, as noted earlier in fourth section of Chapter 1, we do not present this result here since the values may be significantly different when we finish tuning the parameters.

Visualization of structural changes

In this section, we describe the visualization modules (the viz/ directory) in src/indentation, src/stretching and src/shearing (Figure 2-3). Visualization is especially important in the current simulations with ongoing parameter tuning, to double-check simulation results make good sense. Note that a dedicated visualization module for src/diffusion is not made, since we simply track the MSD of the particles without applying indentation or in-plane deformation.

Of the four windows in indent.ovito, two windows are selected to visualize deformation of the global and local CGNE deformation. In first, global deformation is visualized from the side (Figure 4-1a). In the second, local deformations of the monolayer and the meshwork are visualized from the top (Figure 4-1b). The 'Membrane deformation' refers to the z-displacement of monolayer particles. The 'NL filament strain' refers to the strain in nuclear lamin filaments. In these example images, the indenter is shown just touching the membrane.

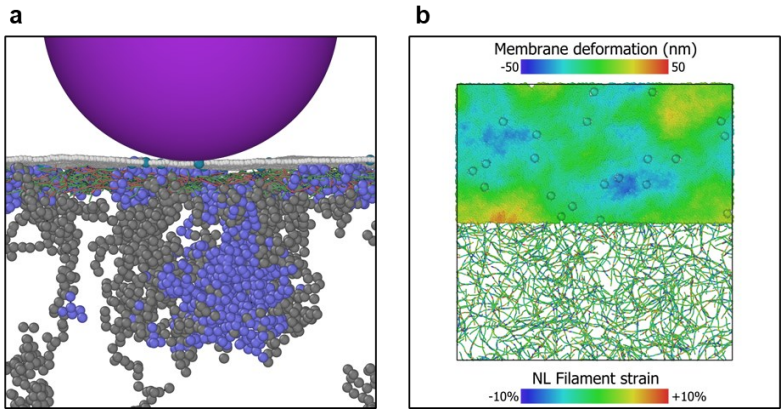

Figure 4-1 Example of visualization of structural change of CGNE under indentation via indent.ovito. **a**, Global deformation visualized in the first window. **b**, Local deformations in the monolayer and meshwork visualized in the second window.

In stretch.ovito, two windows are selected to visualize the global and local CGNE deformations. Since we apply deformation to the entire simulation box, it will be interesting to visualize the local deformations in each nuclear component. To make a neat visualization, we implemented a one-layer-per-quadrant data processing pipeline. It can be seen in Figure 3-2 that the CGNE is a stack of three layers on top of the PC. To make this

easier to see, Figure 3-2d is replotted in Figure 4-2a. The xy-plane can be divided into four Cartesian quadrants. Then, each quadrant can be dedicated to visualize one of the PC, monolayer, NL-B and NL-A (Figure 4-2b). In the first window, the global deformation is visualized in an orthographic projection. In Figure 4-2c, we show this visualization, but at zero deformation for simplicity. In the second window, local deformations in each CGNE layer and the PC are visualized. The 'PC chain strain' refers to the strain in the peripheral chromatin chain. Thickness of NL filaments was doubled to make them easier to see.

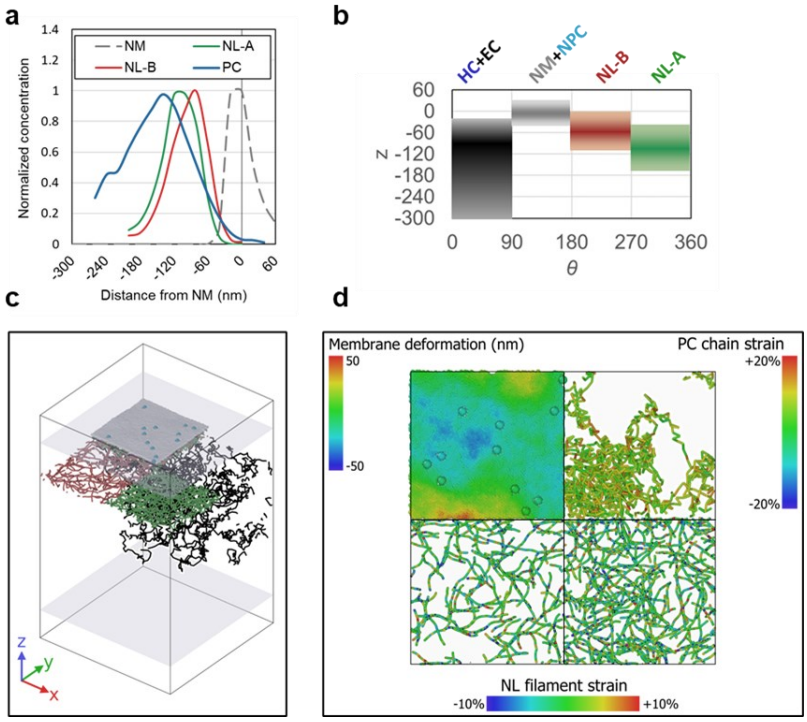

Figure 4-2 Example of visualization of structural change of CGNE under stretching via stretch.ovito. **a**, The 3 stacked layers of CGNE on top of the PC. **b**, Illustration of the one-layer-per-quadrant data processing pipeline. **c**, The first window with orthographic projection of the simulation box. The stacked layers of CGNE are revealed along with PC in a counter-clockwise helical manner. **d**, Local deformations in each CGNE layer and the PC visualized in the second window.

Chapter 5 Parameters of the CGNE

In this chapter, the selection of the model parameters is discussed. A top-down approach is taken starting from the environment, moving towards material composition, then molecular structure of the components, and finishing with the interactions of the components. Several parameters could be chosen within tight bounds guided by experimental data. Some parameters were identified as *tunable parameters* that are being tuned for consistency of viscoelasticity metrics with the experimental data.

Environmental parameters

The simulations were conducted using the latest version of Large-scale Atomic/Molecular Massively Parallel Simulator (LAMMPS). The simulation box comprised a $2.5\ \mu m \times 2.5\ \mu m$ patch of the NE with periodic boundary conditions on the sides, and $1.5\ \mu m$ space above and $3\ \mu m$ below the NM. The top and bottom faces are non-periodic. To avoid potential loss of particles from these faces of the simulation box, reflective walls are placed at $0.5\ \mu m$ into the simulation box from both faces. The monolayer was inserted in the xy-plane. In the $2.5\ \mu m \times 2.5\ \mu m \times 2.5\ \mu m$ region below the xy-plane, the generated meshwork filaments and chain are inserted. The $2.5\ \mu m \times 2.5\ \mu m \times 1.0\ \mu m$ region above the NM was kept empty, i.e., cytoplasmic structures such as F-actin and microtubules are not included.

The masses of the five particle types were estimated as: $m_1 = 2248\ kDa$, $m_2 = 120000\ kDa$, $m_3 = 139\ kDa$, $m_4 = 136\ kDa$, and $m_5 = m_6 = 8950\ kDa$. The calculation of coarse-graining degree are described in the *Compositional parameters* section and the masses are derived from the derivation from experimental data into 'masses' sheet in the src/env.xlsx. The average particle mass $\sum_{i=1}^{6} \frac{m_i N_i}{\sum_{i=1}^{6} N_i}$, where N_i is number of particles of type i, was chosen as the reduced mass, $\tilde{m} = 2174\ kDa$. The hydrodynamic radius of each particle was chosen based on the equilibrium separation in the interaction potentials that the particle was part of: $R_1 = 11\ nm$, $R_2 = 35\ nm$, $R_3 = 6\ nm$, $R_4 = 6\ nm$, and $R_5 = R_6 = 35\ nm$; see the 'masses' sheet in the src/env.xlsx for calculation.

The translational relaxation time, $\tau_t = 0.003\tilde{\tau}$ was chosen by tuning it to achieve experimentally comparable viscosity in the meshwork. For spherical particles, $\tau_r = 0.3\tau_t$ is usually used for correct rotational diffusivity (Dias et al. 2016). However, since the particles are assembled in a monolayer, the rotational viscosity is expected to be small; the background fluid cannot flow around the entire particle which is part of a monolayer. With $\tau_r = 0.3\tau_t$, the monolayer undulations war indeed damped severely. We chose $\tau_r = 30\ \tau_t$, which made the rotational damping negligible compared to translational damping while still being large enough for thermostatting.

The reduced temperature was chosen as $\tilde{T} = 0.23$ so that the membrane is in fluid phase (Yuan et al. 2010). For the temperature $T = 300\text{K}$, the reduced energy (or energy

scale) was therefore $\tilde{\epsilon} = \frac{k_B T}{\tilde{T}} = 1.8 \times 10^{-20}\, J$. Half the equilibrium bond length of NL particles was chosen as the reduced length, $\tilde{\sigma} = 10\, nm$. The time scale was obtained as $\tilde{\tau} = \tilde{\sigma}\sqrt{\tilde{m}/\tilde{\epsilon}} = 4.48\, ns$. The timestep was taken as $\Delta\tau = 0.002\, \tilde{\tau}$, which was found to be small enough to resolve thermal fluctuations of all particles big and small.

Compositional parameters

NM composition: The NM is a particle monolayer with side length, $L = 2.5\, \mu m$. It has 17208 sites with NM and 37 sites with NPCs. In experiments, area density of lipids (in single lipid bilayer) and NPCs (in NM, which is a double lipid bilayer) is $\rho_{L,exp} \approx 2\, nm^{-2}$ (ENGELMAN 1969; Kinnun et al. 2015; Leftin et al. 2014) and $\rho_{NPC,exp} \approx 6\, \mu m^{-2}$ (Turgay et al. 2017), respectively. The $\rho_{NPC,exp}$ can be directly compared with ρ_{NPC} since a single NPC particle in simulations represents a single NPC. The experimental density for mouse embryonic fibroblast (MEF) was used. While $\rho_{L,exp}$ cannot be compared directly, it will be used in a later sub-section on calculations of degree of coarse-graining.

NL composition: The NL is a filament meshwork also with side length, $L = 2.5\, \mu m$. It has several ball-and-stick filaments totaling 23730 particles. About one-third of the particles are NL-B, while the rest are NL-A. This choice was discussed earlier in third section of Chapter 3. The area density of filaments (number of filaments per unit area of NE patch), $\rho_{NL} = 207\, \mu m^{-2}$ was close to that in experiments, $\rho_{NL} = 207\, \mu m^{-2}$ (Turgay et al. 2017).

PC composition: The PC is a chain-of-bead also with side length, $L = 2.5\,\mu m$. It is a single chain totaling 6303 particles. About half of the particles are HC, while the rest are EC.

Coarse-graining degree: Let CG_{LinNM} denote the number of lipids in a single NM particle, and CG_{BinNM} denote the number of lamin-binding proteins (LBPs) in a single NM particle. We did not find any estimate of number density of LBPs on the NM in the literature. Hence, each NM particle contains at most a single LBP and implies that $CG_{BinNM} \approx 1$. The lipid content of the NM particles, CG_{LinNM} can be obtained by calculating the number of lipids in the NM region in two ways: $N_{LinNM} = N_{NM} * CG_{LinNM}$ and, $N_{LinNM} = \rho_{L,exp} * 2 * 2 * (L^2 - N_{NPC}\pi r_{NPC}^2)$. In the first, the number is obtained by multiplying number of NM particles with coarse-grained lipid content of the NM particles. In the second, the number is obtained as a product of $\rho_{L,exp}$ and the area of the two leaflets in the NM region. $(L^2 - N_{NPC}\pi r_{NPC}^2)$ is used to approximate the surface area of this NPC-excluded region. The two multiplications by 2 are because the NM is a double bilayer, while $\rho_{L,exp}$ is the number of lipids per unit area on one side of a bilayer. From the equations gives $CG_{LinNM} \approx 2839$ (see the 'masses' sheet in the src/env.xlsx for the calculation). Since a single NPC is CG by each NPC particle, $CG_{NPC\_in\_NPC} = 1$. Since approximately two lamins are CG by each NL particle, $CG_{Lamins\_in\_NL} = 2$. These were mentioned earlier. Now, about 50 nucleosomes are expected to be CG by a single bead on PC chain. Hence, $CG_{Nuc\_in\_PC} = 50$.

Interaction parameters

The values of the interaction parameters are documented in Table 5-1, which is an extended version of Table 2-1.

Table 5-1 Values of model parameters for various types of interactions

Interaction	Model	Parameter Set	Values (reduced units)
Non-bonded interactions			
NM – NM	Membrane	$\{\epsilon, \sigma, r_c, \zeta, \mu, \theta_0\}$	{1.0, 2.0, 5.2, 4, 5.0, 0.0}
NM – NPC	Membrane	$\{\epsilon, \sigma, r_c, \zeta, \mu, \theta_0\}$	{2.0, 6.0, 9.2, 4, 5.0, 0.0}
NPC – NPC	Mie	$\{\epsilon, \sigma, r_c, m, n\}$	{0.01, 10.61, 15.0, 4, 2}
NL-A – NL-A	Mie	$\{\epsilon, \sigma, r_c, m, n\}$	{0.0075, 0.524, 1.5, 9, 6}
NL-A – NL-B	Mie	$\{\epsilon, \sigma, r_c, m, n\}$	{0.0054, 0.524, 1.5, 9, 6}
NL-B – NL-B	Mie	$\{\epsilon, \sigma, r_c, m, n\}$	{0.0052, 0.524, 1.5, 9, 6}
EC – EC	Mie	$\{\epsilon, \sigma, r_c, m, n\}$	{0.0023, 4.95, 9.8, 9, 6}
EC – HC	Mie	$\{\epsilon, \sigma, r_c, m, n\}$	{0.0115, 4.95, 7.0, 9, 6}
HC – HC	Mie	$\{\epsilon, \sigma, r_c, m, n\}$	{0.0115, 4.95, 12.6, 9, 6}
NM – NL-A	Mie	$\{\epsilon, \sigma, r_c, m, n\}$	{0.0025, 4.368, 6.0, 9, 6}
NM – NL-B	Mie	$\{\epsilon, \sigma, r_c, m, n\}$	{0.0100, 4.368, 6.0, 9, 6}
NPC – NL	Mie	$\{\epsilon, \sigma, r_c, m, n\}$	{0.0075, 8.741, 11.0, 9, 6}
(NM, NPC) – EC	Mie	$\{\epsilon, \sigma, r_c, m, n\}$	{0.0023, 3.536, 5.0, 4, 2}
(NM, NPC) – HC	Mie	$\{\epsilon, \sigma, r_c, m, n\}$	{0.0115, 3.536, 7.0, 4, 2}
NL – EC	Mie	$\{\epsilon, \sigma, r_c, m, n\}$	{0.0115, 3.006, 4.25, 4, 2}
NL – HC	Mie	$\{\epsilon, \sigma, r_c, m, n\}$	{0.0115, 3.006, 5.75, 4, 2}
Bonded interaction			
NL Filament	Harmonic	$\{K, r_0\}$	{150.0, 2.0}
Cross-link (CL)	Morse	$\{D_0, K, r_0\}$	{4.0, 30.0, 1.2}
Transverse-link (TL)	Morse	$\{D_0, K, r_0\}$	{4.0, 2.0, 5.0}
PC Chain	KG	$\{K, R, \epsilon, \sigma\}$	{0.276, 11.2, 0.23, 7.0}
NL Filament	Cosine	$\{L_p, \theta_0\}$	{50, 180°}
Reversible bonding			
CL (NL-A – NL-A)	Create	$\{f_{mk}, r_{mk}, i_{max}, j_{max}, p\}$	{1, 1.44, 3, 3, 0.05}
CL (NL-B – NL-B)	Create	$\{f_{mk}, r_{mk}, i_{max}, j_{max}, p\}$	{1, 1.44, 3, 3, 0.05}
TL (NM – NL-A)	Create	$\{f_{mk}, r_{mk}, i_{max}, j_{max}, p\}$	{1, 5.50, 2, 1, 0.05}
TL (NPC – NL-A)	Create	$\{f_{mk}, r_{mk}, i_{max}, j_{max}, p\}$	{1, 5.50, 5, 1, 0.05}
TL (NM – NL-B)	Create	$\{f_{mk}, r_{mk}, i_{max}, j_{max}, p\}$	{1, 5.50, 2, 1, 0.05}
TL (NPC – NL-B)	Create	$\{f_{mk}, r_{mk}, i_{max}, j_{max}, p\}$	{1, 5.50, 2, 1, 0.05}
CL (all)	Break	$\{f_{brk}, r_{brk}, p\}$	{5, 1.50, 1.00}
TL (all)	Break	$\{f_{brk}, r_{brk}, p\}$	{5, 6.25, 1.00}

Chapter 6 Related Works

In this chapter, works on physical modeling of NE mechanics are discussed. We discuss the contributions and limitations of related works, which helped and motivated this work.

The main factor that motivated the CGNE model presented here is the recent emergence of experimental literature on detailed quantification of: (a) the mechanical response of single lamins (Bera et al. 2014; Qin and Buehler 2011), (b) mechanical response of stretched NE (Dahl et al. 2004; Deviri et al. 2019; Wintner et al. 2020), (c) force-displacement characteristic of NE via AFM (Liu et al. 2014; Nakamura et al. 2004, 2005; Wang et al. 2018; Xia et al. 2018; H. Xie et al. 2018; Yokokawa, Takeyasu, and Yoshimura 2008), (d) structure of single lamins (Makarov et al. 2019; Turgay et al. 2017), (e) structure of nuclear lamina (Nmezi et al. 2019; Turgay et al. 2017; W. Xie et al. 2016), and (f) nuclear membrane and nuclear pore complexes (Beck et al. 2007).

Various theoretical and computational models relevant to NE mechanics have been developed to study the physical behavior of NE components. Extensive work has been done with atomistic-level simulations in unravelling nanoscale mechanisms such as protein unfolding in lamin A Ig domain (Bera et al. 2014), α-helix to β-sheet transition in lamin filaments (Qin and Buehler 2011; Sapra et al. 2020), and transport through NPC (Ghavami et al. 2014; Huang and Szleifer 2020; Mincer and Simon 2011; Moussavi-Baygi et al. 2011). Macroscopic continuum modeling approaches have also been taken to study

supranuclear features such as nuclear volume regulation (Kim et al. 2015), envelope blebbing (Funkhouser et al. 2013), nuclear viscoelasticity (Dahl et al. 2005; Wang et al. 2018), and subnuclear features nuclear membrane porosity (Torbati, Lele, and Agrawal 2016), and nuclear lamina hole nucleation (Deviri et al. 2019). Most of these articles had used experimental data to guide modeling decisions and some decisions in the CGNE model presented here have benefited from such information.

Despite the modeling of nuclear components in these models in unprecedented detail, they are either highly simplified to resolve the nanoscale NE architecture, or highly detailed making them computationally infeasible for simulating the processes that occur on length scales of NE thickness. Among the nanoscale modelling approaches, only a subset of nuclear components has been modeled in detail, neglecting the potential interplay of the components through cooperative interactions. No current model, theoretical or computational, accounts for all significant interactions of subnuclear components in a common framework, leaving much of NE mechanics unexplored and poorly understood. The CGNE model presented here is aimed to address these limitations.

Chapter 7 Closing remarks

In this chapter, the thesis is concluded with comments about the ongoing work planned to be completed in the near future.

Conclusion

In this thesis, we presented a coarse-grained molecular dynamics model of the mammalian NE, referred as the Coarse-Grained Nuclear Envelope (CGNE). The model features the four main nuclear envelope components (nuclear membrane, nuclear pore complex, A-type nuclear lamina and B-type nuclear lamina) along with peripheral chromatin, especially heterochromatin, that interlaces with the nuclear lamina. We presented a three-step protocol that allows generating experimentally consistent CGNE structure. Tuning of interaction parameters is ongoing and we are unable to present, at the moment of preparation of this thesis, CGNE that not only has experimentally consistent structure, but also experimental consistent viscoelastic properties.

Future work

The values of several interaction parameters are not well chosen. Two approaches are being taken to improve these choices: a top-down approach of tuning the parameters for consistency of NE viscoelasticity in simulations and experiments, and a bottom-up approach of continually surveying the literature for experimental insight on certain

molecular interactions parameters that were guessed in lack of availability or our discovery of such data in the literature.

A small but notable improvement of the coarse-grained modeling of LBPs of NM was realized in hindsight. Explicitly identifying certain NM particles as ‘LBP-rich NM’ will be a simpler model of the occasional encounters of the nuclear lamins with LBPs on the NM, than the current model of probabilistic formation of the membrane links.

A manuscript is under development to publish a revised CGNE model with above improvements in the near future.

References

Ahn, Jinsook et al. 2019. "Structural Basis for Lamin Assembly at the Molecular Level." *Nature Communications* 10(1): 1–12.

Allen, Michael P., and Dominic J. Tildesley. 2017. 1 *Computer Simulation of Liquids*. Oxford University Press.

Beaudouin, Joël et al. 2002. "Nuclear Envelope Breakdown Proceeds by Microtubule-Induced Tearing of the Lamina." *Cell* 108(1): 83–96.

Beck, Martin et al. 2007. "Snapshots of Nuclear Pore Complexes in Action Captured by Cryo-Electron Tomography." *Nature* 449(7162): 611–15.

Bera, Manindra et al. 2014. "Characterization of Unfolding Mechanism of Human Lamin A Ig Fold by Single-Molecule Force Spectroscopy—Implications in EDMD." *Biochemistry* 53(46): 7247–58.

Bianco, Simona et al. 2018. "Polymer Physics Predicts the Effects of Structural Variants on Chromatin Architecture." *Nature Genetics* 50(5): 662–67.

Boucher, Pierre Alexandre, Béla Joós, Martin J. Zuckermann, and Luc Fournier. 2007. "Pore Formation in a Lipid Bilayer under a Tension Ramp: Modeling the Distribution of Rupture Tensions." *Biophysical Journal* 92(12): 4344–55.

Brandt, Erik G. et al. 2011. "Interpretation of Fluctuation Spectra in Lipid Bilayer Simulations." *Biophysical Journal* 100(9): 2104–11.

Burley, Stephen K. et al. 2021. "RCSB Protein Data Bank: Powerful New Tools for Exploring 3D Structures of Biological Macromolecules for Basic and Applied Research and Education in Fundamental Biology, Biomedicine, Biotechnology,

Bioengineering and Energy Sciences." *Nucleic Acids Research* 49(D1): D437–51.

Cain, Natalie E. et al. 2014. "The SUN Protein UNC-84 Is Required Only in Force-Bearing Cells to Maintain Nuclear Envelope Architecture." *Journal of Cell Biology* 206(2): 163–72.

Cain, Natalie E., and Daniel A. Starr. 2015. "SUN Proteins and Nuclear Envelope Spacing." *Nucleus* 6(1): 2–7.

Capell, Brian C et al. 2005. "Inhibiting Farnesylation of Progerin Prevents the Characteristic Nuclear Blebbing of Hutchinson-Gilford Progeria Syndrome." *Proceedings of the National Academy of Sciences of the United States of America* 102(36): 12879–84.

Chiang, Michael et al. 2019. "Polymer Modeling Predicts Chromosome Reorganization in Senescence." *Cell Reports* 28(12): 3212-3223.e6.

Chu, Fang-Yi, Shannon C. Haley, and Alexandra Zidovska. 2017. "On the Origin of Shape Fluctuations of the Cell Nucleus." *Proceedings of the National Academy of Sciences* 114(39): 10338–43.

Dahl, Kris Noel, Adam J. Engler, J. David Pajerowski, and Dennis E. Discher. 2005. "Power-Law Rheology of Isolated Nuclei with Deformation Mapping of Nuclear Substructures." *Biophysical Journal* 89(4): 2855–64.

Dahl, Kris Noel, Samuel M Kahn, Katherine L Wilson, and Dennis E Discher. 2004. "The Nuclear Envelope Lamina Network Has Elasticity and a Compressibility Limit Suggestive of a Molecular Shock Absorber." *Journal of cell science* 117(Pt 20): 4779–86.

Damodaran, Karthik et al. 2018. "Compressive Force Induces Reversible Chromatin

Condensation and Cell Geometry–Dependent Transcriptional Response" ed. Valerie Marie Weaver. *Molecular Biology of the Cell* 29(25): 3039–51.

Dechat, Thomas et al. 2010. "Nuclear Lamins." *Cold Spring Harbor Perspectives in Biology* 2(11): a000547–a000547.

Denais, Celine M et al. 2016. "Nuclear Envelope Rupture and Repair during Cancer Cell Migration." *Science* 352(6283): 353–58.

Deviri, Dan et al. 2019. "Scaling Laws Indicate Distinct Nucleation Mechanisms of Holes in the Nuclear Lamina." *Nature Physics*.

Dias, C. S., C. Braga, N. A.M. Araújo, and M. M. Telo Da Gama. 2016. "Relaxation Dynamics of Functionalized Colloids on Attractive Substrates." *Soft Matter* 12(5): 1550–57.

Discher, D. E. et al. 2007. "Physical Plasticity of the Nucleus in Stem Cell Differentiation." *Proceedings of the National Academy of Sciences* 104(40): 15619–24.

Dittmer, Travis, and Tom Misteli. 2011. "The Lamin Protein Family." *Genome Biology* 12(5).

Doi, Masao, and Samuel Frederick Edwards. 1988. *The Theory of Polymer Dynamics*. Clarendon Press.

ENGELMAN, DONALD M. 1969. "Surface Area per Lipid Molecule in the Intact Membrane of the Human Red Cell." *Nature* 223(5212): 1279–80.

Fischer-Cripps, Anthony C. 2007. *Introduction to Contact Mechanics*. 2nd ed. Springer Science+Business Media, LLC.

Funkhouser, Chloe M. et al. 2013. "Mechanical Model of Blebbing in Nuclear Lamin Meshworks." *Proceedings of the National Academy of Sciences* 110(9): 3248–53.

Ghavami, Ali, Liesbeth M. Veenhoff, Erik van der Giessen, and Patrick R. Onck. 2014. "Probing the Disordered Domain of the Nuclear Pore Complex through Coarse-Grained Molecular Dynamics Simulations." *Biophysical Journal* 107(6): 1393–1402.

Gov, N., A. G. Zilman, and S. Safran. 2003. "Cytoskeleton Confinement and Tension of Red Blood Cell Membranes." *Physical Review Letters* 90(22): 228101.

Guelen, Lars et al. 2008. "Domain Organization of Human Chromosomes Revealed by Mapping of Nuclear Lamina Interactions." *Nature* 453(7197): 948–51.

Guilak, Farshid, John R. Tedrow, and Rainer Burgkart. 2000. "Viscoelastic Properties of the Cell Nucleus." *Biochemical and Biophysical Research Communications* 269(3): 781–86.

Huang, Kai, and Igal Szleifer. 2020. "Modeling the Nucleoporins That Form the Hairy Pores." *Biochemical Society Transactions* 48(4): 1447–61.

Isermann, Philipp, and Jan Lammerding. 2013. "Nuclear Mechanics and Mechanotransduction in Health and Disease." *Current Biology* 23(24): R1113–21.

Israelachvili, Jacob. 2011. Intermolecular and Surface Forces *Intermolecular and Surface Forces*. 3rd ed. Elsevier.

Jahed, Zeinab, Mohammad Soheilypour, Mohaddeseh Peyro, and Mohammad R. K. Mofrad. 2016. "The LINC and NPC Relationship – It's Complicated!" *Journal of Cell Science* 129(17): 3219–29.

Kim, D.-H. et al. 2015. "Volume Regulation and Shape Bifurcation in the Cell Nucleus." *Journal of Cell Science* 128(18): 3375–85.

Kind, Jop et al. 2013. "Single-Cell Dynamics of Genome-Nuclear Lamina Interactions." *Cell* 153(1): 178–92.

Kinnun, Jacob J., K.J. Mallikarjunaiah, Horia I. Petrache, and Michael F. Brown. 2015. "Elastic Deformation and Area per Lipid of Membranes: Atomistic View from Solid-State Deuterium NMR Spectroscopy." *Biochimica et Biophysica Acta (BBA) - Biomembranes* 1848(1): 246–59.

Kittisopikul, Mark et al. 2021. "Computational Analyses Reveal Spatial Relationships between Nuclear Pore Complexes and Specific Lamins." *Journal of Cell Biology* 220(4).

Lai, Lipeng, Xiaofeng Xu, Chwee Teck Lim, and Jianshu Cao. 2015. "Stiffening of Red Blood Cells Induced by Cytoskeleton Disorders: A Joint Theory-Experiment Study." *Biophysical Journal* 109(11): 2287–94.

de Leeuw, Rebecca, Yosef Gruenbaum, and Ohad Medalia. 2018. "Nuclear Lamins: Thin Filaments with Major Functions." *Trends in Cell Biology* 28(1): 34–45.

Leftin, Avigdor et al. 2014. "Area per Lipid and Cholesterol Interactions in Membranes from Separated Local-Field (13)C NMR Spectroscopy." *Biophysical journal* 107(10): 2274–86.

Lieberman-Aiden, E. et al. 2009. "Comprehensive Mapping of Long-Range Interactions Reveals Folding Principles of the Human Genome." *Science* 326(5950): 289–93.

Liu, Haijiao et al. 2014. "In Situ Mechanical Characterization of the Cell Nucleus by Atomic Force Microscopy." *ACS Nano* 8(4): 3821–28.

Mahamid, Julia et al. 2016. "Visualizing the Molecular Sociology at the HeLa Cell Nuclear Periphery." *Science* 351(6276): 969–72.

Makarov, Alex A. et al. 2019. "Lamin A Molecular Compression and Sliding as Mechanisms behind Nucleoskeleton Elasticity." *Nature Communications* 10(1):

3056.

van Mameren, Joost, Karen C. Vermeulen, Fred Gittes, and Christoph F. Schmidt. 2009. "Leveraging Single Protein Polymers To Measure Flexural Rigidity." *The Journal of Physical Chemistry B* 113(12): 3837–44.

Mincer, Joshua S., and Sanford M. Simon. 2011. "Simulations of Nuclear Pore Transport Yield Mechanistic Insights and Quantitative Predictions." *Proceedings of the National Academy of Sciences* 108(31): E351–58.

Miron, Ezequiel et al. 2020. "Chromatin Arranges in Chains of Mesoscale Domains with Nanoscale Functional Topography Independent of Cohesin." *Science Advances* 6(39): eaba8811.

Moir, Robert D, Anne D Donaldson, and Murray Stewart. 1991. "Expression in Escherichia Coli of Human Lamins A and C: Influence of Head and Tail Domains on Assembly Properties and Paracrystal Formation." *Journal of cell science* 99 (Pt 2): 363–72.

Moller, D. et al. 2009. "A Progeria Mutation Reveals Functions for Lamin A in Nuclear Assembly, Architecture, and Chromosome Organization." *Proceedings of the National Academy of Sciences* 106(49): 20788–93.

Moussavi-Baygi, Ruhollah, Yousef Jamali, Reza Karimi, and Mohammad R. K. Mofrad. 2011. "Brownian Dynamics Simulation of Nucleocytoplasmic Transport: A Coarse-Grained Model for the Functional State of the Nuclear Pore Complex" ed. Vijay S. Pande. *PLoS Computational Biology* 7(6): e1002049.

Nakamura, Noriyuki et al. 2004. "Mechanical Sensing of the Penetration of Various Nanoneedles into a Living Cell Using Atomic Force Microscopy." *Biosensors and Bioelectronics* 20(8): 1652–55.

Nakamura, Noriyuki et al. 2005. “Nanoscale Operation of a Living Cell Using an Atomic Force Microscope with a Nanoneedle.” *Nano Letters* 5(1): 27–30.

Nmezi, Bruce et al. 2019. “Concentric Organization of A- and B-Type Lamins Predicts Their Distinct Roles in the Spatial Organization and Stability of the Nuclear Lamina.” *Proceedings of the National Academy of Sciences* 116(10): 4307–15.

Osmanagic-Myers, Selma, Thomas Dechat, and Roland Foisner. 2015. “Lamins at the Crossroads of Mechanosignaling.” *Genes & Development* 29(3): 225–37.

Panorchan, Porntula, Benjamin W. Schafer, Denis Wirtz, and Yiider Tseng. 2004. “Nuclear Envelope Breakdown Requires Overcoming the Mechanical Integrity of the Nuclear Lamina.” *Journal of Biological Chemistry* 279(42): 43462–67.

Qin, Zhao, and Markus J. Buehler. 2011. “Flaw Tolerance of Nuclear Intermediate Filament Lamina under Extreme Mechanical Deformation.” *ACS Nano* 5(4): 3034–42.

Rowat, Amy C., Jan Lammerding, Harald Herrmann, and Ueli Aebi. 2008. “Towards an Integrated Understanding of the Structure and Mechanics of the Cell Nucleus.” *BioEssays* 30(3): 226–36.

Sapra, K. Tanuj et al. 2020. “Nonlinear Mechanics of Lamin Filaments and the Meshwork Topology Build an Emergent Nuclear Lamina.” *Nature Communications* 11(1): 6205.

Schmidt, Christine S. et al. 2013. “LBR and Lamin A/C Sequentially Tether Peripheral Heterochromatin and Inversely Regulate Differentiation.” *Cell* 152(3): 584–98.

Schreiber, Katherine H., and Brian K. Kennedy. 2013. “When Lamins Go Bad: Nuclear Structure and Disease.” *Cell* 152(6): 1365–75.

Schreiner, Sarah M. et al. 2015. “The Tethering of Chromatin to the Nuclear Envelope

Supports Nuclear Mechanics." *Nature Communications* 6(1): 7159.

Sengupta, Kaushik et al. 2013. "Viscoelastic Behavior of Human Lamin A Proteins in the Context of Dilated Cardiomyopathy." *PLoS ONE* 8(12): e83410.

Shah, Pragya, Katarina Wolf, and Jan Lammerding. 2017. "Bursting the Bubble – Nuclear Envelope Rupture as a Path to Genomic Instability?" *Trends in Cell Biology* 27(8): 546–55.

Shimi, Takeshi et al. 2008. "The A- and B-Type Nuclear Lamin Networks: Microdomains Involved in Chromatin Organization and Transcription." *Genes & Development* 22(24): 3409–21.

Shimi, Takeshi et al. 2015. "Structural Organization of Nuclear Lamins A, C, B1, and B2 Revealed by Superresolution Microscopy." *Molecular Biology of the Cell* 26(22): 4075–86.

van Steensel, Bas, and Andrew S Belmont. 2017. "Lamina-Associated Domains: Links with Chromosome Architecture, Heterochromatin, and Gene Repression." *Cell* 169(5): 780–91.

Steinkühler, Jan et al. 2019. "Mechanical Properties of Plasma Membrane Vesicles Correlate with Lipid Order, Viscosity and Cell Density." *Communications Biology* 2(1): 337.

Stephens, Andrew D. et al. 2017. "Chromatin and Lamin a Determine Two Different Mechanical Response Regimes of the Cell Nucleus." *Molecular Biology of the Cell* 28(14): 1984–96.

Struglinski, Mark J., and William W. Graessley. 1985. "Effects of Polydispersity on the Linear Viscoelastic Properties of Entangled Polymers. 1. Experimental Observations

for Binary Mixtures of Linear Polybutadiene." *Macromolecules* 18(12): 2630–43.

Swift, J., and D. E. Discher. 2014. "The Nuclear Lamina Is Mechano-Responsive to ECM Elasticity in Mature Tissue." *Journal of Cell Science* 127(14): 3005–15.

Swift, Joe et al. 2013. "Nuclear Lamin-A Scales with Tissue Stiffness and Enhances Matrix-Directed Differentiation." *Science* 341(6149): 1240104.

Tajik, Arash et al. 2016. "Transcription Upregulation via Force-Induced Direct Stretching of Chromatin." *Nature Materials* 15(12): 1287–96.

Torbati, Mehdi, Tanmay P. Lele, and Ashutosh Agrawal. 2016. "Ultradonut Topology of the Nuclear Envelope." *Proceedings of the National Academy of Sciences* 113(40): 11094–99.

Turgay, Yagmur et al. 2017. "The Molecular Architecture of Lamins in Somatic Cells." *Nature* 543(7644): 261–64.

Ulianov, Sergey V. et al. 2019. "Nuclear Lamina Integrity Is Required for Proper Spatial Organization of Chromatin in Drosophila." *Nature Communications* 10(1): 1176.

Ungricht, Rosemarie, and Ulrike Kutay. 2017. "Mechanisms and Functions of Nuclear Envelope Remodelling." *Nature Reviews Molecular Cell Biology* 18(4): 229–45.

Wang, Xian et al. 2018. "Mechanical Stability of the Cell Nucleus – Roles Played by the Cytoskeleton in Nuclear Deformation and Strain Recovery." *Journal of Cell Science* 131(13): jcs209627.

Webster, M., K. L. Witkin, and O. Cohen-Fix. 2009. "Sizing up the Nucleus: Nuclear Shape, Size and Nuclear-Envelope Assembly." *Journal of Cell Science* 122(10): 1477–86.

Wei, Fanan et al. 2016. "Poroelasticity of Cell Nuclei Revealed through Atomic Force

Microscopy Characterization." *Applied Physics Letters* 109(21).

Wilson, Katherine L, and Roland Foisner. 2010. "Lamin-Binding Proteins." *Cold Spring Harbor perspectives in biology* 2(4): a000554–a000554.

Wintner, Oren et al. 2020. "A Unified Linear Viscoelastic Model of the Cell Nucleus Defines the Mechanical Contributions of Lamins and Chromatin." *Advanced Science* 7(8).

Xia, Yuntao et al. 2018. "Nuclear Rupture at Sites of High Curvature Compromises Retention of DNA Repair Factors." *Journal of Cell Biology* 217(11): 3796–3808.

Xie, Hui, Jianmin Song, Xianghe Meng, and Hao Zhang. 2018. "In Situ Quantification of the Young's Modulus of Nuclei In Multiple Cellular States Using A Modified Fiber Probe Sensor." *IEEE Sensors Journal* PP(X): 1.

Xie, Wei et al. 2016. "A-Type Lamins Form Distinct Filamentous Networks with Differential Nuclear Pore Complex Associations." *Current Biology* 26(19): 2651–58.

Yokokawa, M, K Takeyasu, and S H Yoshimura. 2008. "Mechanical Properties of Plasma Membrane and Nuclear Envelope." *Journal of Microscopy* 232(August 2007): 82–90.

Yuan, Hongyan et al. 2010. "One-Particle-Thick, Solvent-Free, Coarse-Grained Model for Biological and Biomimetic Fluid Membranes." *Physical Review E - Statistical, Nonlinear, and Soft Matter Physics* 82(1): 1–8.

Zhou, Min. 2003. "A New Look at the Atomic Level Virial Stress: On Continuum-Molecular System Equivalence." *Proceedings of the Royal Society of London. Series A: Mathematical, Physical and Engineering Sciences* 459(2037): 2347–92.